Naval Research Laboratory

Washington, DC 20375-5320

NRL/MR/6040--17-9762

Computational Fluid Dynamics Studies of Blast Loading on Helmeted Warfighters

David R. Mott

Laboratory for Multiscale Reactive Flow Physics
Laboratories for Computational Physics and Fluid Dynamics

Douglas A. Schwer

Laboratory for Propulsion, Energetic, and Dynamic Systems
Laboratories for Computational Physics and Fluid Dynamics

Theodore R. Young

Berkeley Research Associates
Beltsville, Maryland

December 22, 2017

REPORT DOCUMENTATION PAGE

Form Approved
OMB No. 0704-0188

1. REPORT DATE *(DD-MM-YYYY)*	**2. REPORT TYPE**	**3. DATES COVERED** *(From - To)*
22-12-2017	Memorandum Report	

4. TITLE AND SUBTITLE

Computational Fluid Dynamics Studies of Blast Loading on Helmeted Warfighters

5a. CONTRACT NUMBER

5b. GRANT NUMBER
64-9310-A4-5

5c. PROGRAM ELEMENT NUMBER

6. AUTHOR(S)

David R. Mott, Douglas A. Schwer, and Theodore R. Young*

5d. PROJECT NUMBER

5e. TASK NUMBER

5f. WORK UNIT NUMBER

7. PERFORMING ORGANIZATION NAME(S) AND ADDRESS(ES)

Naval Research Laboratory
4555 Overlook Avenue, SW
Washington, DC 20375-5320

8. PERFORMING ORGANIZATION REPORT NUMBER

NRL/MR/6040--17-9762

9. SPONSORING / MONITORING AGENCY NAME(S) AND ADDRESS(ES)

Naval Research Laboratory
4555 Overlook Avenue, SW
Washington, DC 20375-5320

10. SPONSOR / MONITOR'S ACRONYM(S)

11. SPONSOR / MONITOR'S REPORT NUMBER(S)

12. DISTRIBUTION / AVAILABILITY STATEMENT

Approved for public release; distribution is unlimited.

13. SUPPLEMENTARY NOTES

*Berkeley Research Associates Inc., 6537 Mid Cities Ave., Beltsville, MD 20705

14. ABSTRACT

This work collects the project reports provided to Marine Corps Systems Command (MCSC) over the years 2009 through 2014 documenting computational fluid dynamics (CFD) studies of blast impingement on helmeted warfighters. The reports were in support of the Infantry Combat Equipment Development and Evaluation program for Program Manager – Infantry Combat Equipment (PM-ICE). The appendix also includes an article which appeared in the proceedings for the 2008 Military Aspects of Blast and Shock (MABS) conference held in Oslo, Norway, which was also provided to PM-ICE and serves as the lead report in the series.

15. SUBJECT TERMS

CFD	TBI	IED
Helmet	Underwash	
Blast	Confined	

16. SECURITY CLASSIFICATION OF:			**17. LIMITATION OF ABSTRACT**	**18. NUMBER OF PAGES**	**19a. NAME OF RESPONSIBLE PERSON**
a. REPORT	**b. ABSTRACT**	**c. THIS PAGE**			David R. Mott
Unclassified Unlimited	Unclassified Unlimited	Unclassified Unlimited	Unclassified Unlimited	74	**19b. TELEPHONE NUMBER** *(include area code)* (202) 767-1974

Standard Form 298 (Rev. 8-98)
Prescribed by ANSI Std. Z39.18

This page intentionally left blank.

CONTENTS

EXECUTIVE SUMMARY

This work collects the project reports provided to Marine Corps Systems Command (MCSC) over the years 2009 through 2014 documenting computational fluid dynamics (CFD) studies of blast impingement on helmeted warfighters. The reports were in support of the Infantry Combat Equipment Development and Evaluation program for Program Manager – Infantry Combat Equipment (PM-ICE). The appendix also includes an article which appeared in the proceedings for the 2008 Military Aspects of Blast and Shock (MABS) conference held in Oslo, Norway, which was also provided to PM-ICE and serves as the lead report in the series.

The collection of reports documents significant progress in predicting and understanding blast loading on realistic head-helmet geometries for a variety of blast scenarios and variations in geometry. Over the course of the work, the primary insights developed include:

1. Blast pressures infiltrate the gap between the helmet brim and head, leading to complex wave interaction and localized pressure amplification on the surface of the head.
2. Including a torso geometry (i.e., not considering a head geometry in isolation) is critical to predicting representative loadings from realistic blast events. In a representative IED scenario with the blast source lower than the head, the pressures that wash over the face and under the helmet depend critically on how the blast wave reflects form the torso.
3. The details of the suspension system (e.g., pads, posts) are very significant in how the waves that infiltrate the gap between the helmet and head interact and subsequently produce elevated pressures.
4. Elevated maximum pressures can result from waves reflected from other adjacent surfaces (such as walls or equipment) if the surfaces are very close to the head, such as standing within 0.5m from the corner of a room. At larger distances, waves reflected from these surfaces typically act as sequential loads on the head – in other words, the waves are spaced in time such that the initial blast wave has passed before secondary reflections reach the head.

This collection of reports was assembled because much of this data and analysis was generated specifically for MCSC and not documented in archival sources. Although the 2008 MABS paper is included in the proceedings of that international conference, accessibility to that archive is uncertain, and so that article is also included here to ensure access and establish context for the other work.

Computational Fluid Dynamics Studies of Blast Loading on Helmeted Warfighters

1. INTRODUCTION

The defense, medical, and research communities have pursued ways to identify, predict, and prevent Mild Traumatic Brain Injury (mTBI) in our service members. These injuries are frequently associated with blasts from improvised explosive devices (IEDs). [1.1,1.2]

Marine Corps Systems Command (MCSC) sponsored a series of studies at the Naval Research Laboratory (NRL) that included determining the pressure loading on a helmeted Marine for a variety of blast scenarios and helmet geometries. The studies were in support of the Infantry Combat Equipment Development and Evaluation program for Program Manager – Infantry Combat Equipment (PM-ICE). The Program Manager at MCSC directing the work was John O'Donnell.

This work collects the project reports provided to PM-ICE over the years 2009 through 2014 that document computational fluid dynamics (CFD) studies of blast impingement on helmeted warfighters. The appendix includes an article which appeared in the proceedings for the 2008 Military Aspects of Blast and Shock (MABS) conference held in Oslo, Norway [1.3], which was also provided to MCSC in 2008 and serves as the lead report in the series.

1.1 Background

Combining computational studies with blast experiments is a powerful approach for gaining insight into complex physical phenomena. Well-done experiments provide a ground truth to anchor understanding, and the computational exploration often provides data that is difficult or impossible to capture experimentally. Once the simulation approach is sufficiently validated and verified, sequences of calculations enable parameter studies that would be impractical to pursue experimentally.

One such study began in 2008 [1.3,1.4]. Open-field blast experiments using a Marine Corps Lightweight Helmet (LWH) and Hybrid II mannequin were compared to calculations based on the Army's Advanced Combat Helmet (ACH). In these initial computations, a realistic three-dimensional head and shoulder geometry and a simplified torso were used, and only the helmet shell (i.e., no liner or suspension) was included. The geometry was assumed stiff and rigid, and no material response in the head, body, or helmet was considered. The flows about the geometry and the subsequent surface loadings were calculated for blasts approaching from the front, side, and rear. The charge size and placement were chosen to represent a dismounted IED scenario.

The authors described the infiltration of the pressure waves and flow into the gap between the helmet and head, subsequently called the "underwash," [1.5] and they identified the wave reflections and interactions that generated pressure peaks about the head that were driving the flow field and were captured in the experimental data. The authors concluded that at specific locations (that depend on the geometry and blast orientation) the peak pressures can increase due to the trapping of waves by the helmet, but that overall the helmet mitigates the blast loading on the head [1.3,1.4]. Later study including optional helmet equipment such as a face shield and mandible protector demonstrated both the underwash effect as well as the critical role that reflections from the torso can have in characterizing the loadings experienced by the helmet and head. [1.6,1.7]

The series of studies describe herein are the continued computational exploration of the blast parameter space enabled by the initial partnership between computation and experiment in 2008. The studies consider the effects of changing computational grid resolution, blast strength, helmet suspension design, and proximity to walls, and the results build a body of knowledge about the loading generated from blast events.

Manuscript approved October 3, 2017.

Other researchers explored similar blast events with coupled fluid-structure models including transmission of loads into and through the head and helmet. Moss et al. studied the coupled fluid-structure interaction problem using a simplified three-dimensional body and helmet geometry. [1.5] They found that in their model that skull flexure, and not head acceleration as in typical blunt impact loading, was the primary source of the mechanical load in the brain. They also describe the underwash affect, which was pronounced for their sling-style suspension but abated by their foam suspension. They found that the foam suspension did, however, couple the helmet motion more strongly to the head and increase the mechanical loading in the brain in their model.

Ganpule et al.[1.8] conducted computational studies of the load transmission to a two-dimensional, circular "head" with and without an arc-shaped helmet, to study how a discreet, localized pressure pulse applied to a small region on one side of the geometry generated stresses inside the geometry. Ganpule and collaborators later studied realistic three-dimensional head-helmet geometries subjected to a planar blast wave approaching the head from the front using both computational and experimental techniques. [1.9,1.10] They also studied the effect of curvature and gap width on the wave propagation in two-dimensional gaps. They verified the existence of the underwash effect previously observed by other researchers, and they found that tight-fitting pads that completely block the circumference of the head-helmet gap can prevent the largest pressures from developing. Increasingly detailed analysis of subsequent results [1.10] emphasized how the shape of the head critically affects the flow field about the head, and consequently, the loading on the head. The authors also concluded that biomechanical loading in the brain is dictated by wave transmission from the environment, wave reflections from tissue-material interfaces, and structural deformations. The work reinforced the possibility of skull flexure, proposed by Moss et al., as well as tissue cavitation, as possible injury mechanisms.

1.2 Roadmap for the Current Collection

Each subsequent section in this report is one progress report in the sequence submitted to MCSC on CFD modeling of blast impingement on helmeted heads. The reports span the years 2009 through 2014. Formatting has been updated from that originally submitted to MCSC, but each section is treated as a self-contained entity with separate reference list. This is not an exhaustive collection of all computational work related to military helmets conducted by NRL's Laboratories for Computational Physics and Fluid Dynamics during this time, as some work was published in the open literature, including some work that was supported by the U.S. Army - Natick Soldier Research & Development Center (NSRDC) [1.6,1.7]. This report does, however, document important progress in the understanding of the blast loading phenomena and a growing appreciation of how the details of the geometry and environment can radically change the loading on the head during a blast event.

1.3 Acknowledgments for the Collection

The research was sponsored by Marine Corps Systems Command (MCSC), Program Manager – Infantry Combat Equipment (PM-ICE), as part of the Infantry Combat Equipment Development and Evaluation Program. The authors would like to thank program manager John O'Donnell for his support. The authors would also like to acknowledge the primary investigators for the effort at NRL, first Graham Hubler and then, upon his retirement, Peter Matic.

REFERENCES

1.1. K.H. Taber, D.L. Warden & R.A. Hurley, Blast-related Traumatic Brain Injury , Journal of Neuroscience – Clinical Neuroscience, Spring 2006, Vol. 18, Issue 2, pp 141-145.

1.2. E.G. Blackman, M.E. Hale & S.H. Lisanby, Toward Improving TBI Protection Measures and Standards for Combat Helmets, Institute for Defense Analyses, Defense Science Study Group, 2006 – 2007 Papers.

1.3. D. R. Mott, D. A. Schwer, T. R. Young, Jr., J. Levine, J.–P. Dionne, A. Makris, G. Hubler, 2008. "Blast-Induced Pressure Fields Beneath a Military Helmet," *Proceedings of the 20th International Symposium on Military Aspects of Blast and Shock*, September 1st – 5th, Oslo, Norway.

1.4. D. R. Mott, D. A. Schwer, T. R. Young, Jr., J. Levine, J.–P. Dionne, A. Makris, G. Hubler, 2008. "Blast-Induced Pressure Fields Beneath a Military Helmet," 61st Annual Meeting of the American Physical Society (APS) Division of Fluid Dynamics (DFD), November 23-25, 2008, San Antonio, TX.

1.5. W.C. Moss, M.J. King, E.G. Blackman, 2009. "Skull Flexure from Blast Waves: A Mechanism for Brain Injury with Implications for Helmet Design." *Physical Review Letters,* Vol. 103, Issue 10, Article Number 108702 DOI: 10.1103/PhysRevLett.103.108702.

1.6. DR Mott, DA Schwer, TR Young, Jr., 2012. "Predicting and Mitigating Blast Loading on the Head Beneath a Military Helmet," *Proceedings of the 22nd International Symposium on Military Aspects of Blast and Shock*, November 4 – 9, Bourges, France.

1.7. DR Mott, DA Schwer, TR Young, Jr., "Blast Loading on the Head Under a Military Helmet: Effect of Face Shield and Mandible Protection." 52nd Aerospace Sciences Meeting, AIAA SciTech Forum, (AIAA 2014-0948), National Harbor, MD. https://doi.org/10.2514/6.2014-0948.

1.8. S. Ganpule, L.X. Gu, G.X. Cao, N. Chandra, 2010. "The Effect Of Shock Wave On A Human Head" IMECE2009: *Proceedings Of The ASME International Mechanical Engineering Congress And Exposition*, Vol 2, pps: 339-346, 2010.

1.9. S. Ganpule, L.X. Gu, G.X. A. Alai, N. Chandra, 2012. "Role of helmet in the mechanics of shock wave propagation under blast loading conditions." *Computer Methods in Biomechanics and Biomedical Engineering*, Vol. 15 Issue 11 pp. 1233-1244, DOI:10.1080/10255842.2011.597353, 2012.

1.10. S. Ganpule, A. Alai, E. Plougonven, N. Chandra, "Mechanics of blast loading on the head models in the study of traumatic brain injury using experimental and computational approaches." *Biomechanics and Modeling in Mechanobiology* (2013) 12:511–531, DOI 10.1007/s10237-012-0421-8.

2. HIGHER-INTENSITY BLASTS

Blast Modeling Progress Report: Higher-Intensity Blasts

Prepared for Marine Corps System Command – PM-ICE
In support of project: Infantry Combat Equipment Development and Evaluation
PI: Graham Hubler, Naval Research Laboratory Code 6365

Authors: David Mott, Doug Schwer, and Ted Young, NRL Code 6400
Prepared: November 16, 2009

2.1 Summary

Computational studies of the effect of blast impingement on helmeted-head geometries had previously considered only low-intensity blasts (~1.5 bar overpressure) at the threshold of pulmonary injury. Additional calculations have been performed to determine the qualitative and quantitative differences between the physics of these low-intensity blasts and higher-intensity blasts (~3.5 bar overpressure) for a combination of explosive charge size and standoff distance that results in 50% survivability. The general wave structure in the free-field and the wave transmission between the head and helmet observed in the low-intensity blasts are also present in the higher-intensity case, but the maximum pressures experienced along the head and helmet surfaces for the high-intensity blast increase by a factor ranging from 2.4 to 3.9 compared to the low-intensity case.

2.2 Test Conditions

Figure 2.1 shows the helmet-head-torso geometry, which is identical to model used in previous calculations [2.1]. The geometry is based on the shape of the Advanced Combat Helmet (ACH), but includes no supporting sling structure or pads. There is an uninterrupted gap of about 2.3 cm between the head and the helmet. The model assumes that the head and helmet are rigid and unmoving. Experimental results indicate that movement of the mannequin subjected to similar blast conditions occurs on a significantly longer timescale than the initial blast interaction, supporting the use of this assumption for calculating the blast loading.

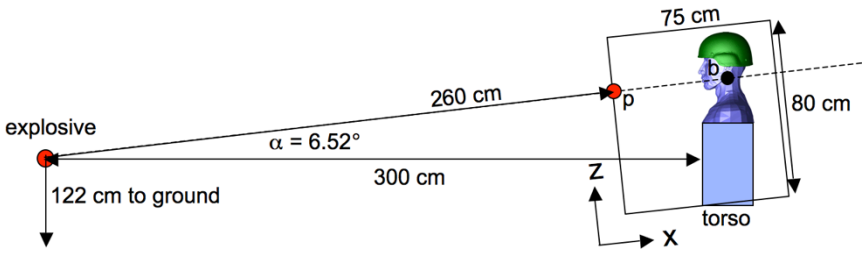

Figure 2.1: Geometry for the Front-Facing blast

Figure 2.2 provides the theoretical peak pressure and positive phase duration for several combinations of charge size and stand off distance as determined by CONWEP [2.2] with respect to the blast injury curves set forth by Bass et al. [2.3]. Previous calculations for 1.5 kg C4 at 3 meter stand off fall below this threshold for pulmonary injury, but this case was of interest for potential TBI effects. The current calculations consider 5 kg C4 at this same stand off distance, which places the blast at 50% survivability.

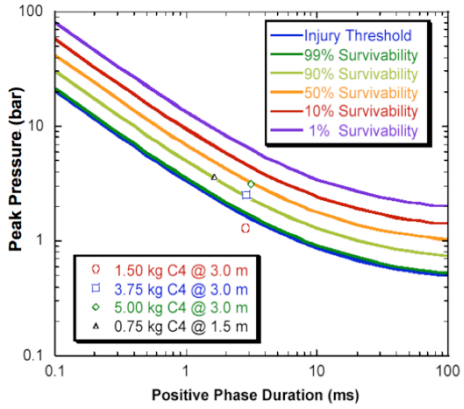

Figure 2.2 Blast Injury curves

As in the previous studies, several orientations relative to the source of the blast were modeled. This report focuses on a

blast approaching the geometry from the front. As in previous testing, the calculation combines an axisymmetric reacting-flow model for predicting the blast profile including ground bounce, and then this data provides boundary conditions for a three-dimensional model of the complex head-helmet geometry. The details of this approach were documented previously [2.1] and are not repeated here.

2.3 Results

Figure 2.3 compares the peak pressure distribution about the helmeted head for the front-facing blast for the low-intensity and high-intensity cases. Red bars indicate the peak pressure at each location for 5.0 kg C4 at 3.0 meters, and blue bars indicate the peak pressures at each location for the 1.5 kg case. The same general behavior is observed in both cases and has been discussed previously [2.1]. The exposed eye sensor experiences a significantly higher pressure than the adjacent forehead locations that are protected from a direct hit from the incident wave. The high pressure generates a wave that penetrates the gap and travels underneath the helmet. Simultaneously, the shock wave travels around the perimeter of the body and helmet and penetrates the gap between the head and helmet. These waves intersect under the helmet on the back of the head, resulting in high peak pressures away from the source of the blast (sensor location CBh2 in Fig. 2.3.) The low- and high-intensity cases are qualitatively the same, but the details of these wave interactions produce some variations in the scaling for the peak pressures between the cases. The high-intensity case produces peak pressures ranging from 2.5 to 3.9 times that of the corresponding peaks in the low-intensity case. Additionally, the highest peak pressure for the 5.0 kg case was measured at the eye, in contrast to the 1.5 kg case for which the highest peak pressure is on the back of the head. In both cases, the peaks at these two locations are comparable, and subtle differences in how the waves beneath the helmet interact generate a slightly lower pressure than the direct reflection on the eye.

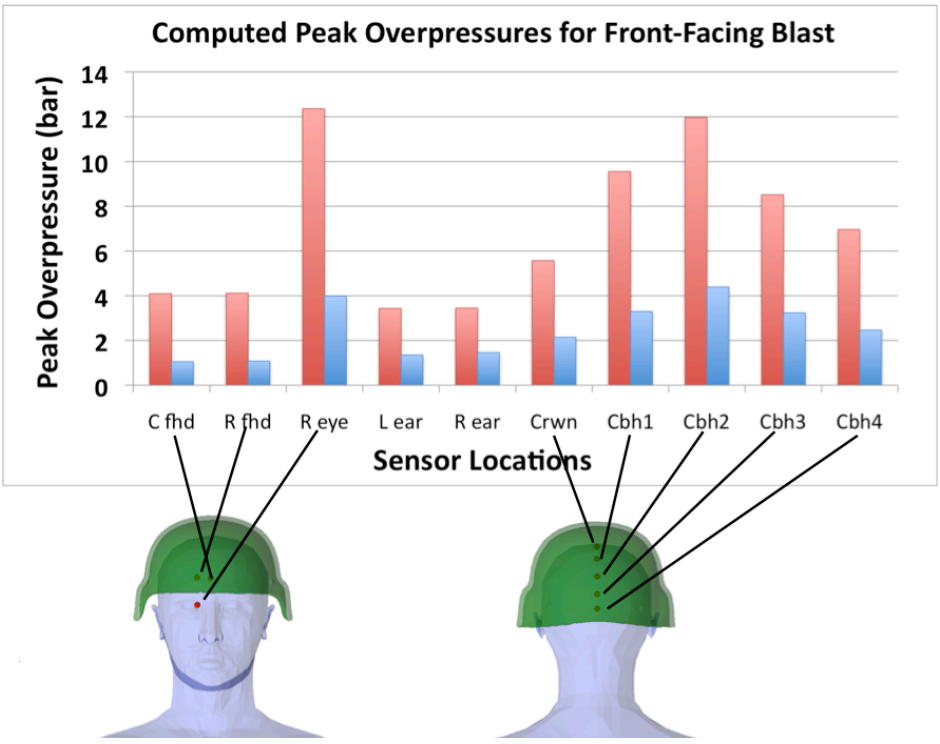

Figure 2.3: Peak overpressure for the low-intensity blast (blue) and the high-intensity blast (red).

2.4 Conclusions

Computational studies for 5.0 kg C4 at 3 m stand off were conducted for a variety of blast orientations, and the details of the front-facing blast are included here. In all cases, the interaction of the wave with the helmeted-head geometry is similar to that of the lower-intensity blasts, including the infiltration of waves in the gap between the helmet and head, and the generation of a higher peak pressure away from the source of the explosion that is comparable to the peak experienced by an unprotected surface exposed to the incident wave. A 2.5-fold increase in the incident wave strength produced a factor of 2.4 to 3.9 increase in the local peak pressure at various locations on the head.

REFERENCES

[2.1] D. R. Mott, D. A. Schwer, T. R. Young, Jr. J. Levine, J.–P. Dionne, A. Makris, G. Hubler, "Blast-Induced Pressure Fields Beneath a Military Helmet," Proceedings of the 20th International Symposium on Military Aspects of Blast and Shock, September 1st – 5th, 2008, Oslo, Norway.

[2.2] C Kingery & G Bulmarsh, *Airblast Parameters from TNT Spherical Air Burst and Hemispherical Surface Burst*. ARBRL-TR-02555, US Army Ballistic Research Laboratory, Aberdeen Proving Ground, MD., 1984.

[2.3] CR Bass, K Rafaels & R Salazar, *Pulmonary Injury Risk Assessment for Short-Duration Blasts*, Proceedings from the Personnel Armour Systems Symposium PASS 2006, Leeds, U.K., September 18th-22nd, 2006

3. COMUTATIONAL RESOLUTION TESTING

Blast Modeling Progress Report: Computational Resolution Testing

Prepared for Marine Corps System Command – PM-ICE
In support of project: Infantry Combat Equipment Development and Evaluation
PI: Graham Hubler, Naval Research Laboratory Code 6365

Authors: David Mott, Doug Schwer, and Ted Young, NRL Code 6400
Submitted: November 17, 2009

3.1 Summary

Computational studies of blast impingement on helmeted-head geometries have been performed at two levels of grid refinement in order to determine an adequate resolution for modeling the flow physics. The computational results are also compared to experimental data to better gauge what level of detail the modeling captures, and how differences between the computational geometry and the experimental mannequin affect the results. Good agreement is seen between the high-resolution and lower-resolution calculations, but the maximum pressures vary ~5-10% between the cases. The higher-resolution calculation can resolve sharper, higher peaks, and details of the wave propagation, particularly the precise locations where the waves intersect under the helmet, likely contribute to these differences as well. Differences between the experimental pressure measurements and the calculated values are more significant than the differences between the computational results at the two grid resolutions. These differences are likely due to the presence of the face shield in the experiments and the absence of the support structure between the head and helmet in the computations. The lower of the two tested resolutions provides sufficient detail for modeling the current geometry, but the issue will be revisited as blast modeling including the support structure matures.

3.2 Computational and Experimental Models

Figure 3.1 shows the computational and experimental helmet-head geometries, which are identical to those used in previous studies [3.1]. The computational geometry is based on the shape of the Advanced Combat Helmet (ACH), but includes no supporting sling structure or pads. There is an uninterrupted gap of about 2.3 cm between the head and the helmet. The baseline (lower-resolution) grid employs 0.25 cm cells around the helmeted-head. This resolution results in 8-10 cells in the gap between the head and the helmet. The higher-resolution grid uses 0.125 cm cells, doubling the resolution in each

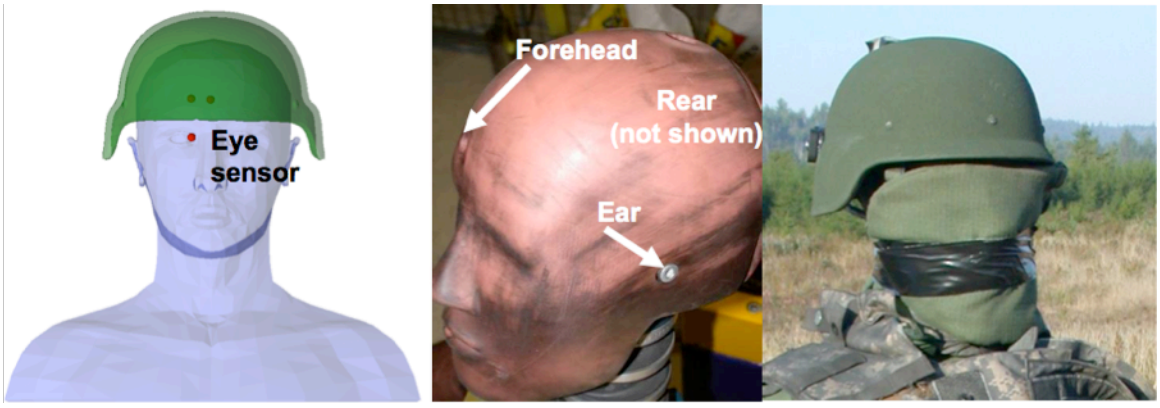

Figure 1 Computational and Experimental Head geometries. Left: computational model. Center: Hybrid III mannequin. Right: mannequin with Nomex face shield

direction. A typical grid for the baseline case (depending upon the blast orientation) consists of ~12 million computational cells. The typical grid for the high-resolution calculation consists of more than 90 million cells.

Figure 3.1 also shows the modified Hybrid III mannequin used in related experimental work performed by Allen-Vanguard Technologies, Inc. [3.1] Gauges recorded the pressure history at the marked locations, and Fig.1 also shows the mannequin prepared for testing. A Nomex cover was placed on the face of the mannequin to protect the mannequin's skin from the repeated blasts. The helmet used in the experiments is the Marine Corps Light Weight Helmet (LWH) with a standard pad support system.

As in the previous studies, several orientations relative to the source of the blast were modeled on both the baseline and high-resolution grids. This report highlights results for blasts approaching the geometry from a 45° angle (i.e., approaching the left cheek). As in previous testing, the calculation combines an axisymmetric reacting-flow model for predicting the blast profile including ground bounce, and then this data provides boundary conditions for a three-dimensional model of the complex head-helmet geometry. The details of this approach were documented previously [3.1] and are not repeated here.

3.3 Results

Figure 3.2 compares the eye-sensor pressure trace as a function of time for the baseline computation and the high-resolution computation to the forehead sensor in the experiment. This data is for the 45° orientation of a blast generated by a 1.5 kg C4 charge at 3 meter stand off distance. The experimental sensor is higher on the head than the eye location indicated in Fig. 3.1, but the helmet and face shield were positioned such that the sensor was exposed to the incident blast. Ambiguity in the precise placement of these items likely accounts for some of the discrepancies between the results of the computations and the experiments.

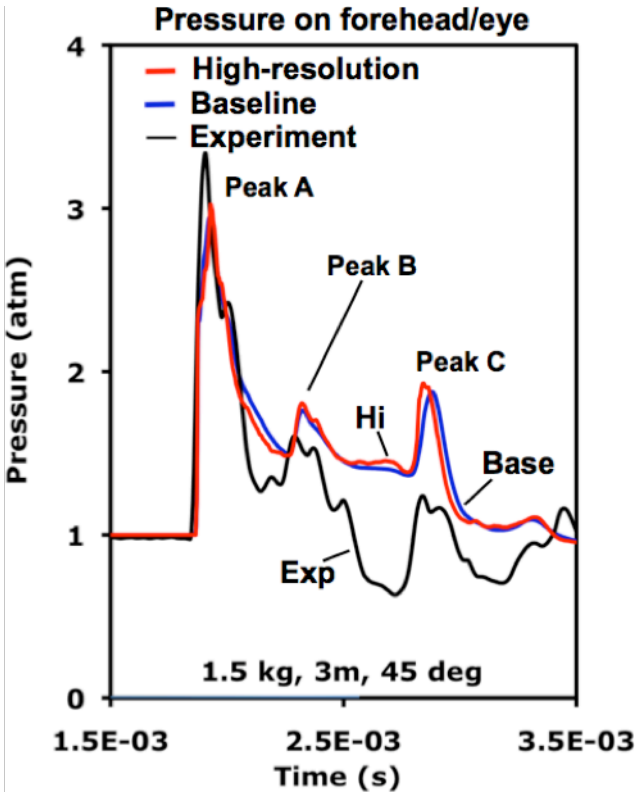

Figure 3.2 pressure traces on the eye and forehead for the 45° orientation.

The three peaks observed in the pressure curves in Fig. 3.2 can be directly linked to the blast wave and its reflections interacting with the geometry. The first peak (Peak A) coincides to the initial blast wave arriving unabated at the sensor location. This wave reflects from the exposed surface producing the pressure spike. This incident wave also strikes the body, producing a reflected wave that travels up from the chest and across the face, generating Peak B. High pressure from the reflected waves penetrates the gap between the head and helmet at the forehead and travels underneath the helmet toward the rear. Simultaneously, the shock wave travels around the perimeter of the head and helmet and penetrates the gap between the head and helmet. These waves intersect under the helmet at the back of the head, producing a high-pressure region that drives a wave back toward

the forehead. This wave generates Peak C as it exits the helmet. This same three-peak structure is seen in the experimental data, suggesting that the primary wave behavior is being captured correctly. However, differences between the computational geometry and the experiment lead to significant differences in the values of these peak pressures.

Figure 3.3 shows a comparison between the peak pressure values at various locations on the head for the baseline resolution and high-resolution cases for the 45° orientation. Red bars indicate the peak pressure at each location for the high-resolution case, and blue bars indicate the peak pressures at each location for the baseline resolution. As discussed previously [3.1], the exposed eye sensor experiences a significantly higher pressure than the adjacent forehead locations that are protected from a direct hit from the incident wave. Locations on the crown and the back of the head experience different peak pressures depending upon their placement relative to where the waves intersect at the back of the head. The higher-resolution calculation consistently predicts slightly higher peak pressures at the various locations since it can better resolve the sharp gradients at the wave fronts. The lower resolution case smears these sharp discontinuities a bit and predicts slightly lower peaks. The most significant difference in peak pressure between the baseline and high-resolution calculations occurs at the back of the head. This difference is likely a combination of sharpening the peak in the high-resolution calculation as well as a change in where the waves focus on the head. These results suggest that the baseline resolution is sufficient for capturing the essential flow physics of the problem and predict peak pressures within approximately 5-10%, but that additional sensor locations should be monitored to ensure that the highest pressures are captured in the diagnostics.

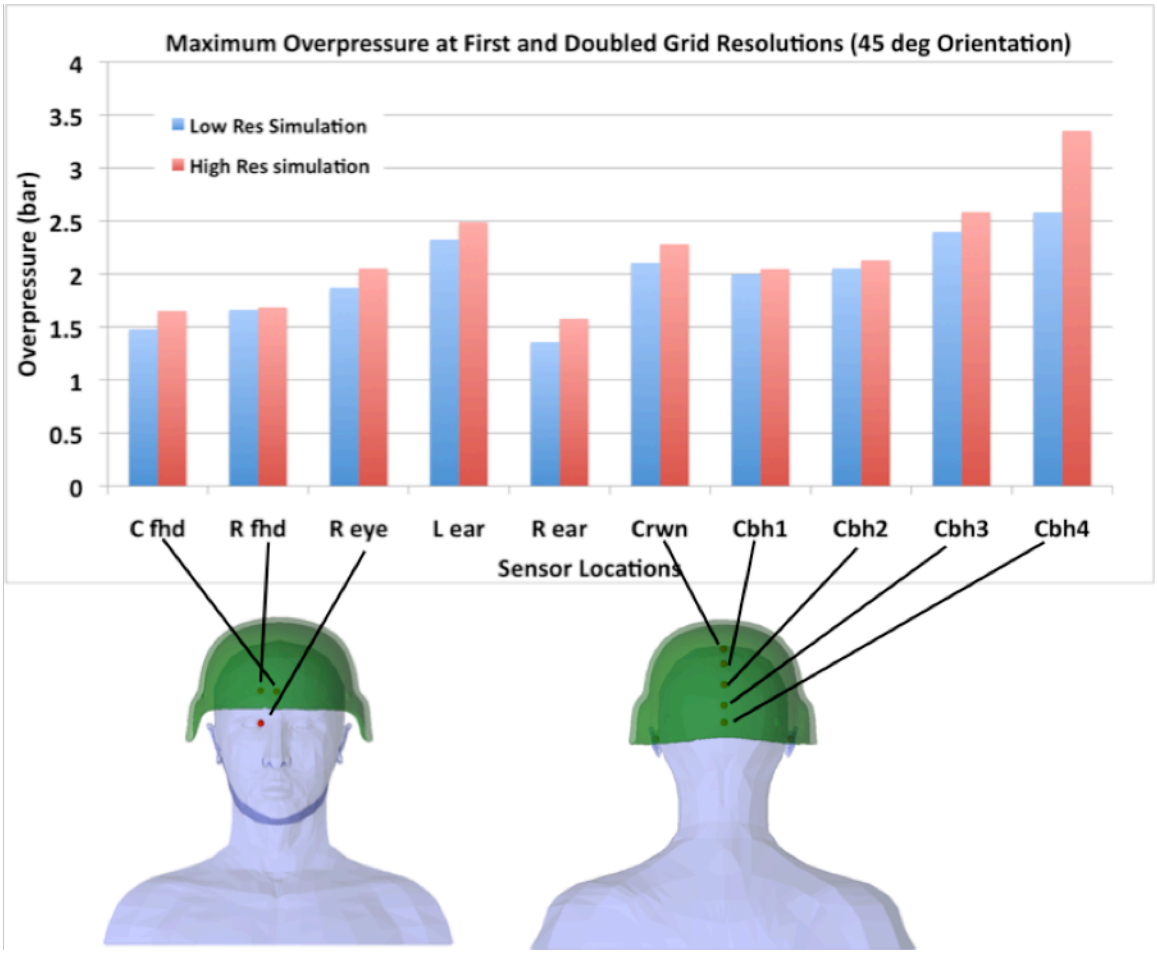

Figure 3.3 Peak pressures at various locations on the head for the 1.5 kg, 3 meter stand off, 45° orientation case. Red bars indicate higher-resolution results. Blue bars indicate the baseline resolution results.

3.4 Conclusions

Computational studies for 1.5 kg C4 at 3 m stand off were conducted for a variety of blast orientations at two grid resolutions, and the results compared to each other and to experiment. Differences between the experimental geometry and computational geometry lead to significant differences in the pressure histories, but the three-peak structure of the experimental results is observed and explained using the computational data. The level of agreement between the baseline and high-resolution calculations suggests that the baseline resolution is sufficient for understanding the physics of the current model system, but this issue will be revisited as realistic models for the pad suspension system mature.

REFERENCES

[3.1] D. R. Mott, D. A. Schwer, T. R. Young, Jr. J. Levine, J.–P. Dionne, A. Makris, G. Hubler, "Blast-Induced Pressure Fields Beneath a Military Helmet," Proceedings of the 20th International Symposium on Military Aspects of Blast and Shock, September 1st – 5th, 2008, Oslo, Norway.

4. INITIAL PAD SUPPORT MODELING

Blast Modeling Progress Report: Initial Pad Support Modeling

Prepared for Marine Corps System Command – PM-ICE
In support of project: Infantry Combat Equipment Development and Evaluation
PI: Graham Hubler, Naval Research Laboratory Code 6365

Authors: David Mott, Doug Schwer, and Ted Young, NRL Code 6400
Submitted: December 10, 2010

4.1 Summary:

Computational studies of blast impingement on helmeted-head geometries including the upper torso have been performed including modeling of the standard Marine Corps Pad-based suspension system. In this work the pad structures are assumed rigid. The primary observations and conclusions are:

1. The highest pressures on the model geometry occurred on unprotected surfaces facing the blast, particularly where the body has some concavity. For example, for a blast originating from the front of the model, the eyes and front of the neck experience the highest peak pressures.
2. Peak pressures under the helmet are similar in magnitude to peak pressures in the previous calculations for which an open gap exists between the head and helmet. However, the presence of the pads alters the locations of the highest peak pressures by reinforcing in some places and in other places interfering with shock wave interactions in the gap between the helmet and the head.
3. Incorporating realistic material properties for the pads in the simulation is expected to reduce the peak pressures predicted under the helmet compared to calculations including rigid pads (the current work) or no pads (previous work). Realistic pads would produce non-ideal reflection of waves at pad surfaces and non-ideal transmission of waves through the pad material.

4.2 Pad Suspension Geometry

Geometry of the pads was provided by Natick Soldier Systems Center in the form of surface coordinates obtained by a three-dimensional scan of each pad. The scan included only the surface of each pad that faces away from the helmet shell when installed. A model of each pad was then generated using analytical functions that reproduced the overall shape of each pad's surface but had the advantage of providing a simple, watertight discretization suitable for implementation within a fluid dynamics calculation. Figure 4.1 shows a photograph of a Marine Corps Light Weight Helmet (LWH) with the pads installed, as well as two views of the computational model of the helmet with pads installed.

The previous studies of the helmet without pads included the collection of pressure histories at various stations under the helmet. Many of these stations were subsequently blocked then the pads were included, so a new set of stations that interrogates the space between the pads, head, and helmet shell were chosen for study. Figure 4.2 displays this new set of forty-four data points, including seven on the torso and neck between the chest and chin, both eyes, both ears, six along the back of the neck outside the helmet, and twenty-seven distributed under the helmet shell.

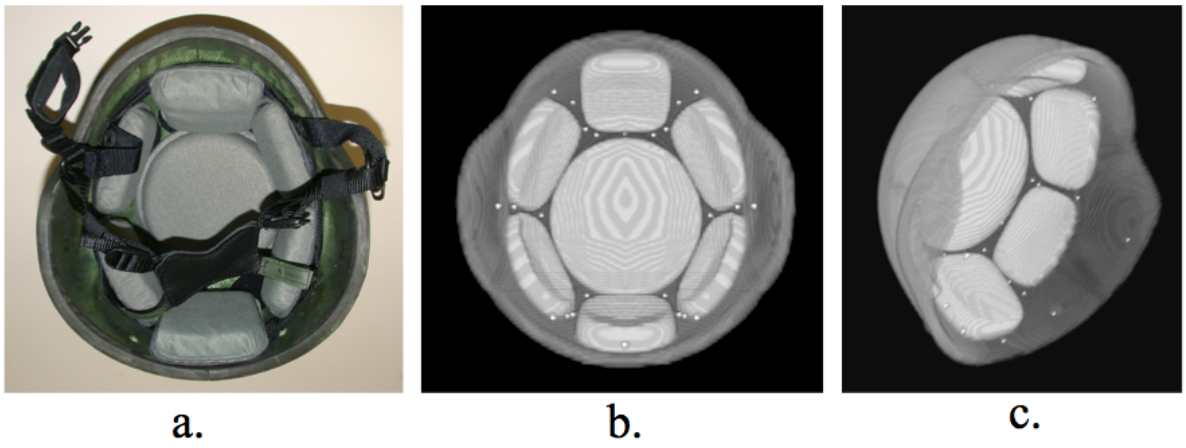

Figure 4.1 Pad configuration for the Marine LWH. a) photograph of installed pads; b) and c) images (at different angles than Fig. 1a) of the three-dimensional model used in the simulation. Bright dots in b and c indicate sensor locations in the computational study that is described in detail in the following section.

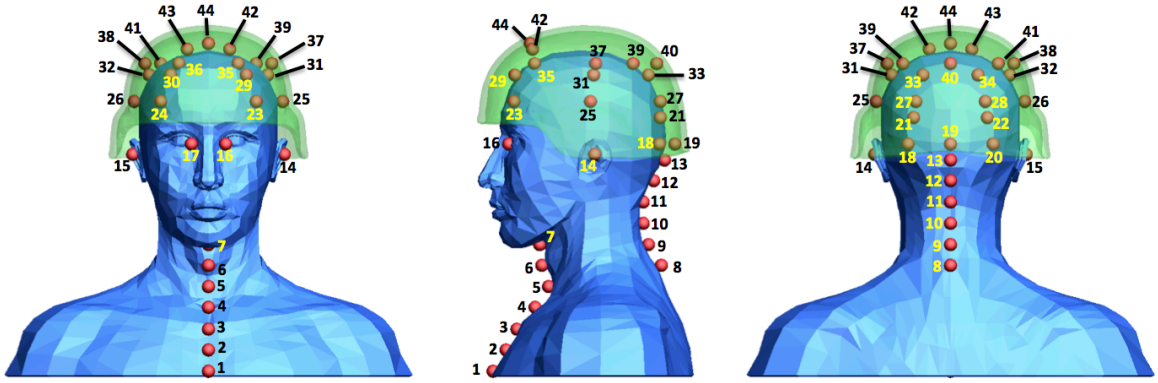

Figure 4.2 Locations at which pressure histories were recorded in the current study.

4.3 Results

Blast strengths corresponding to two standard pulmonary injury thresholds were tested: 50% survivability, corresponding to 5 kg of C4 at 3m standoff distance, and 99% survivability, corresponding to 1.5 kg of C4 at 3m standoff [4.1]. The blast source lies in front of the model.

4.3.1 Exposed Torso and Front of Neck: Stations 1 – 7

Figure 4.3 shows the overpressure for the first 7 sensor locations, placed along the model centerline and running from the chest to under the chin.

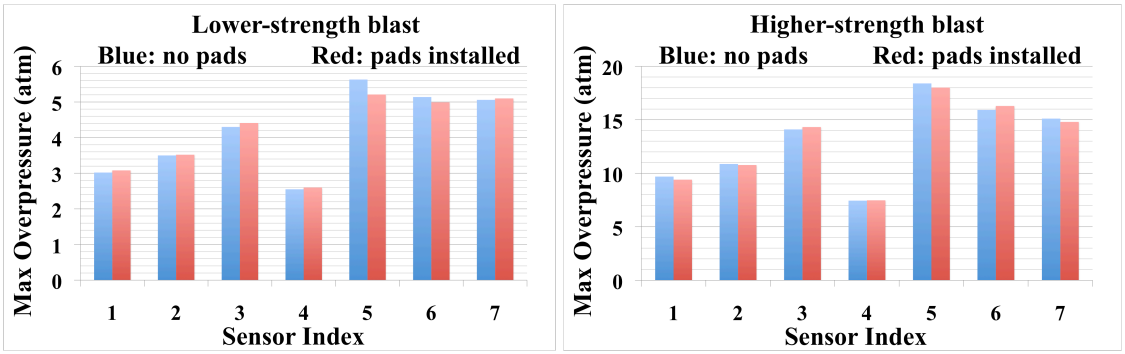

Figure 4.3 Overpressure on exposed neck and torso locations for the lower-intensity (left) and higher-intensity (right) blasts.

This region is directly exposed to the incoming blast wave, and the peak pressures correspond to the arrival of the wave. The peak pressure at each of the locations differs by roughly a factor of 3 between the high-intensity and low-intensity cases. The peak pressure on location 4 is lower than locations 1-3 because the chest slopes such that the wave strikes this point more obliquely than the points further down the torso. The highest peak pressure for this collection of points is at location 5, where the concavity of the neck generates some focusing of the pressure waves and amplifies the peak pressure. Modest differences between the cases including pads and without pads are caused by the numerical nature of the simulation. In the real system, the peak pressure occurs at a particular instant in time, and the numerical calculation generates pressure data at discreet times that may not coincide precisely with the maximum. Since the simulations use adaptive time step control, two separate simulations (such as one with pads and one without) will calculate the pressure at slightly different times in the neighborhood of the peak, and hence return slightly different values for the peak.

4.3.2 Exposed Neck Away from Blast: Stations 8-13

Figure 4.4 shows the overpressure at stations 8 through 13, which run along the model centerline along the back of the neck. As with stations 1 through 7, the data for the higher-intensity blast echoes that of the lower-intensity blast, just at a higher scale. Peak pressures at locations 12 and 13 increase significantly for the cases including pads; the increase for the high-strength blast is approximately a factor of 2. Location 13 is just below the helmet (see Fig 1), and waves enveloping the model penetrate this gap between the helmet and head. When no pads are present, these waves continue under the helmet shell until they interact with other waves that penetrated

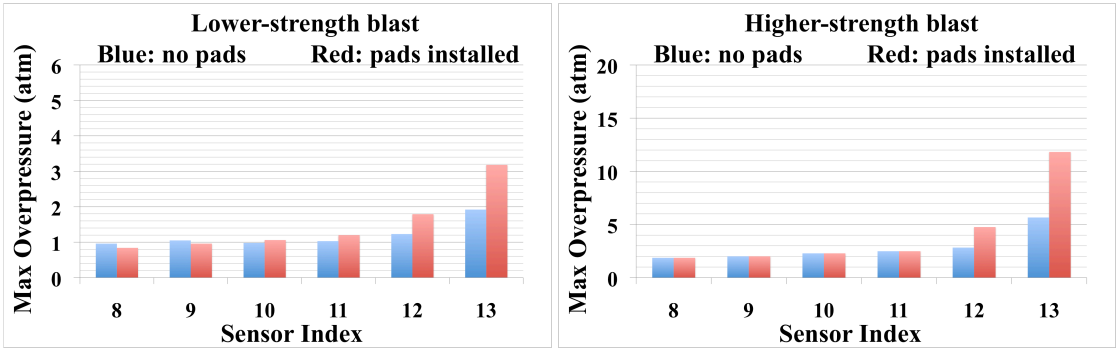

Figure 4.4 Overpressure on exposed locations on the back of the neck (i.e., away form the blast source) for the lower-intensity (left) and higher-intensity (right) blasts.

the gap from other directions. With the rigid pads in place, these waves immediately reflect off the rear pad and generate a higher pressure at location 13. At this location, therefore, the peak pressures for the

two simulations (pads versus no pads) likely bound the more realistic case in which the pad material would allow partial transmission of the wave through the pad.

4.3.3 Eyes, Ears, and Lowest Stations Covered by the Helmet: Stations 14-20

Figure 4.5 shows the peak pressures at the ears (14 and 15), eyes (16 and 17), and three locations across the back of the head (18, 19, and 20) barely covered by the helmet.

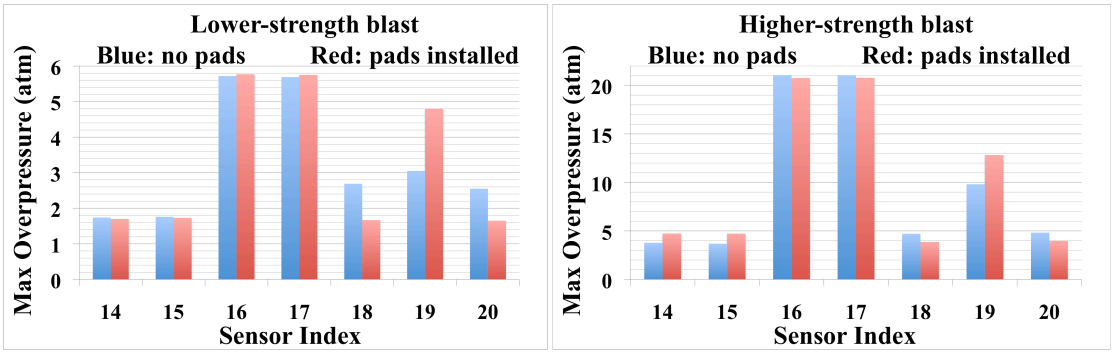

Figure 4.5 Overpressure on ears (14, 15), eyes (16,17), and along the lower part of the back of the head (18, 19, 20) for the lower-intensity (left) and higher-intensity (right) blasts.

The eyes receive the largest overpressures of all the stations tracked, with the higher-pressure blast generating overpressures of over 20 atmospheres. Overpressures on the ears are affected by some modest wave reflections but are relatively consistent between using pads and no pads.

The remaining stations (18, 19, and 20) show the effect of the pads. With no pads installed, these three locations experience two primary pressure spikes. As the external blast wave envelops the geometry, waves infiltrate the gap between the helmet and the head all around the circumference of the head. The infiltrating wave entering under the back of the helmet generates the first pressure spike experienced by these three points.

These penetrating waves then travel within the gap until they intersect close to the crown of the head. This intersection generates a high pressure under the helmet that sends a shock wave back toward the bottom edges of the helmet. The wave produces a second spike in the pressures at points 18, 19, and 20. For point 19, the initial penetrating wave is the stronger of the two spikes. For points 18 and 20, the second wave that is generated by the waves colliding under the helmet produces the higher pressure of the two.

When the pads are installed, station 19 sits just below the rear pad. The initial penetrating wave reflects from the pad and generates a single pressure spike that is larger than the initial penetrating wave alone, hence increasing the maximum overpressure. In contrast, the peak pressures at points 18 and 20 decrease when the pads are present because the pads interfere with the intersecting waves that generated the larger secondary spike at these locations when no pads are installed.

4.3.4 Under the Helmet: Stations 21-44

Figure 4.6 shows the overpressures for the remaining 24 stations distributed throughout the space between the helmet shell, head, and pads.

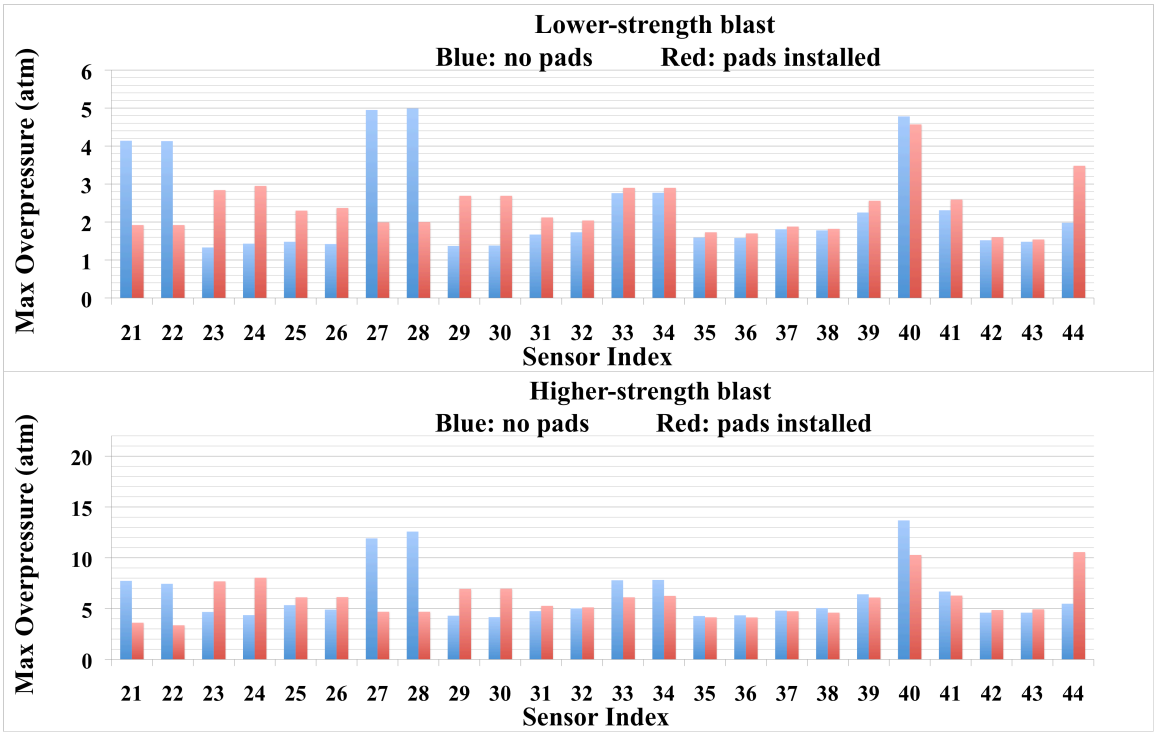

Figure 4.6 Overpressure for the stations under the helmet for the lower-intensity (top) and higher-intensity (bottom) blasts.

Several stations, such as 21 and 22, and 27 and 28, exhibit the same behavior described above for points 18 and 20. With no pads, the highest peak pressure at these locations is generated by the secondary wave produced when the infiltrating waves intersect. The presence of the pads disrupts this wave interaction process at these points and therefore the pads reduce the peak overpressure. At points like 23 and 24, reflections from the pads increase the pressure and channel the waves into the narrow gaps between the pads. Modest initial and secondary peaks seen at positions like 29, 30, and 44 are replaced with a more significant initial peak due to the increased pressures generated by the reflections between the pads.

4.4 Conclusions

The highest peak pressures on the surface of the head and torso lie on unprotected areas of the body directly exposed to the blast, particularly locations such as the eyes that are concave. Through wave interaction between the helmet shell and the head, peak pressures on the head reach levels as high as other exposed areas such as the chest in a front-facing blast. The presence of rigid pads between the head and helmet alters the distribution of peak pressures on the head but does not significantly change the peak pressure values under the helmet. Incorporating realistic material properties for the pads is expected to reduce the peak pressures predicted under the helmet compared to rigid pads or no pads due to non-ideal reflection of waves at pad surfaces and transmission of waves through the pad material.

REFERENCES

[4.1] D. R. Mott, D. A. Schwer, T. R. Young, Jr. J. Levine, J.–P. Dionne, A. Makris, G. Hubler, "Blast-Induced Pressure Fields Beneath a Military Helmet," Proceedings of the 20th International Symposium on Military Aspects of Blast and Shock, September 1st – 5th, 2008, Oslo, Norway.

5. EFFECT OF CHANGING SHELL AND SUSPENSION GEOMETRIES

Blast Modeling Progress Report:
Effect of Changing Shell and Suspension Geometries

Prepared for Marine Corps System Command – PM-ICE
In support of project: Infantry Combat Equipment Development and Evaluation
PI: Graham Hubler, Naval Research Laboratory Code 6365

Authors: David Mott, Doug Schwer, and Ted Young, NRL Code 6040
Submitted: November 30, 2011

5.1 Summary:

Computational studies of blast impingement on helmeted-head geometries including the upper torso have been performed using both the Army Advanced Combat Helmet (ACH) and Marine Corps Lightweight Helmet (LWH). These studies included cases with no intervening suspension (in order to isolate the effect of the helmet shape on pressure infiltration and wave interaction in the limit of very-soft pad suspension) and alternatively included a suspension based on the design of Schubert that consists of an array of approximately 130 posts.

The primary conclusions of this study include:

1. As in previous studies, the highest pressures on the model geometry occurred on unprotected surfaces facing the blast, particularly where the body has some concavity. For example, for a blast originating from the front of the model, the eyes and front of the neck experience the highest peak pressures.

2. The peak pressures under the helmet were modestly higher for the Marine Corps LWH compared to the Army ACH, particularly for the front-facing blast. This result is likely due to the brim capturing slightly more of the incoming wave and directing it under the helmet. However, the brim provides significant mitigation to the peak pressures applied to the eyes, dropping the overpressure from 25 atmospheres to 19 atmospheres in the case presented. This mitigation is very dependent on helmet placement and the location of the blast source.

3. The post suspension interferes with the pressure waves that infiltrate the perimeter of the helmet in a manner that generally reduces the maximum pressure under the helmet relative to the cases with no suspension geometry. Comparisons have not yet been made with the existing pad suspension system with realistic pad material properties, but the potential for using the post-based suspension to mitigating peak under-helmet pressures, relative to using very-stiff and very-soft pad supports, is confirmed.

5.2 ACH and LWH Geometries

Geometry of both helmet shells were provided by Natick Soldier Systems Center in the form of surface coordinates obtained by a three-dimensional scan of each helmet. The separate inner and outer helmet surfaces were spliced together to produce a closed (i.e., "watertight") model of each helmet shell suitable for incorporating into the fluid dynamics simulations. Figure 5.1 shows each helmet geometry in profile as installed on the model head.

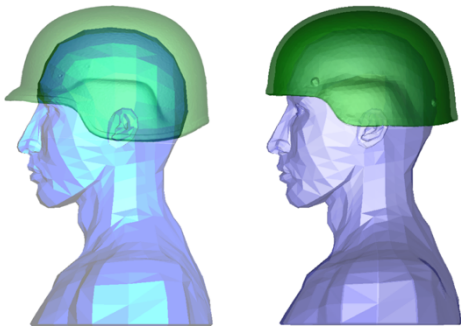

Figure 5.1 Marine LWH (left) and Army ACH (right) geometries.

Pressure time histories were stored and analyzed for 56 stations on the torso, neck, and head. Figure 5.2 shows the locations of these stations. The set includes seven on the torso and neck between the chest and chin, both eyes, both ears, six along the back of the neck outside the helmet, and thirty-nine distributed under the helmet shell.

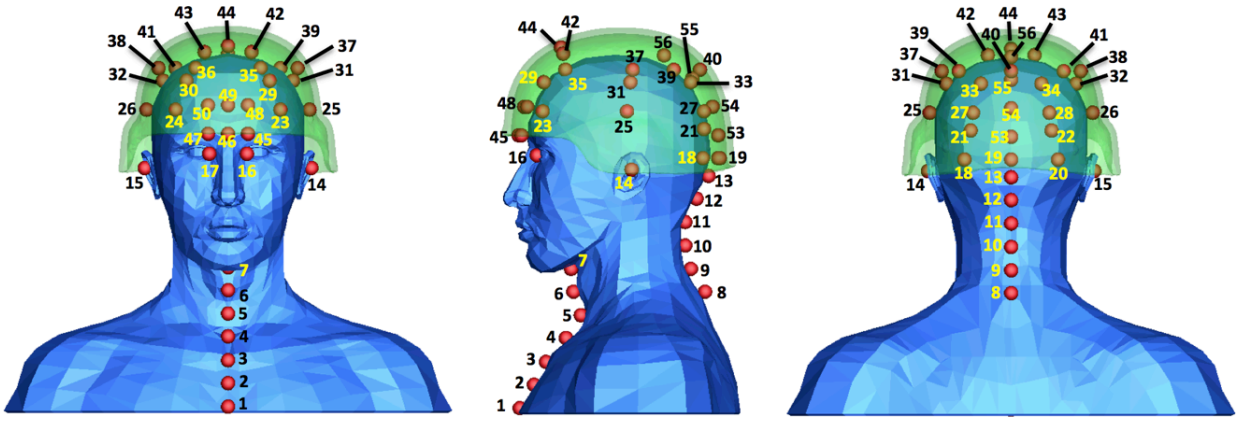

Figure 2 Locations at which pressure histories were recorded in the current study.

5.3 Results

Blast strength corresponding to 50% survivability based on pulmonary injury threshold [5.1] was tested, corresponding to 5 kg of C4 at 3-meter standoff distance [5.2]. This scenario generates a blast wave with an overpressure of ~3.5 atmospheres when it reaches the torso. Blasts were calculated that approached the model from the front, from a 45 deg angle (i.e., approaching the right cheek), from the side, and from behind.

5.3.1 Comparing the ACH and LWH

The flow physics for both helmets is very similar to that previously studied. As the blast wave envelops the body, pressure waves infiltrate the gap between the helmet and the head. This penetration occurs first on the side facing the blast source, but as the wave surrounds the head, pressure waves enter the gap all around the head perimeter. These waves intersect under the helmet and generate high pressures on the head, typically on the side away from the blast source. The focus of this report is to determine if differences between the ACH and LWH geometries (and, in a later section, determine if the post-based suspension) produces significant differences in this process that affects the peak pressures.

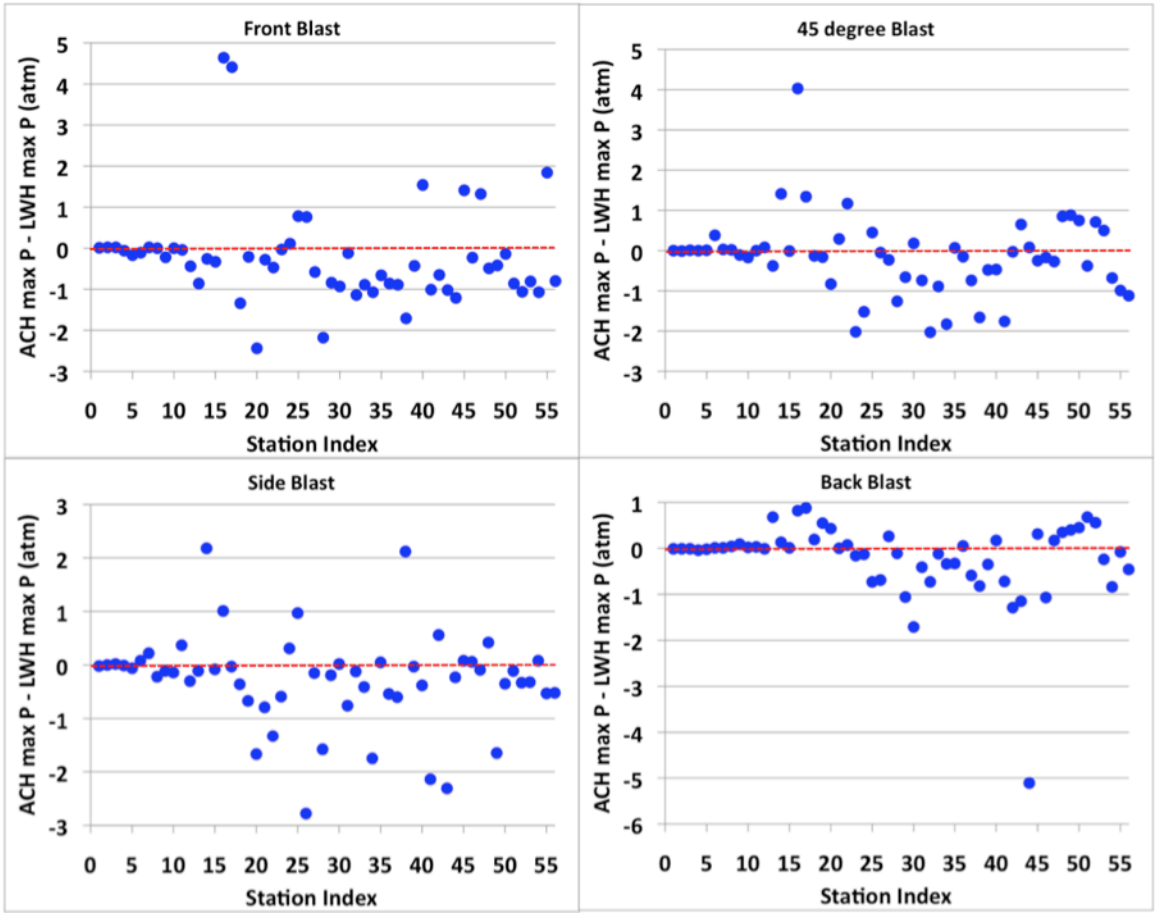

Figure 5.3 Difference in peak pressures between the Army ACH and Marine Corps LWH at each sensor location and for four blast orientations. Values above 0: ACH pressure is higher; values below 0: LWH pressure is higher

Before examining the pressure histories at individual points, an overall assessment of the two geometries can be determined from Figure 5.3. For each of the four blast orientations, the maximum pressure at each sensor location was recorded for both the ACH and the LWH. Peak pressures for all sensor locations and configurations are included in the appendix. Figure 5.3 shows the difference between these maximum pressures between the two helmets. Values above 0 indicate locations where the peak pressure is higher for the ACH than the LWH; data points with values below zero indicate that the peak pressure for the LWH was higher. More data points appear below the horizontal axis, indicating higher pressures under the LWH, but most of these points are within 1 atmosphere of this axis A few notable exceptions are studied in more detail below: the pressures on the eyes (stations 16 and 17) for the front-facing blast, and station 44 for the back-facing blast.

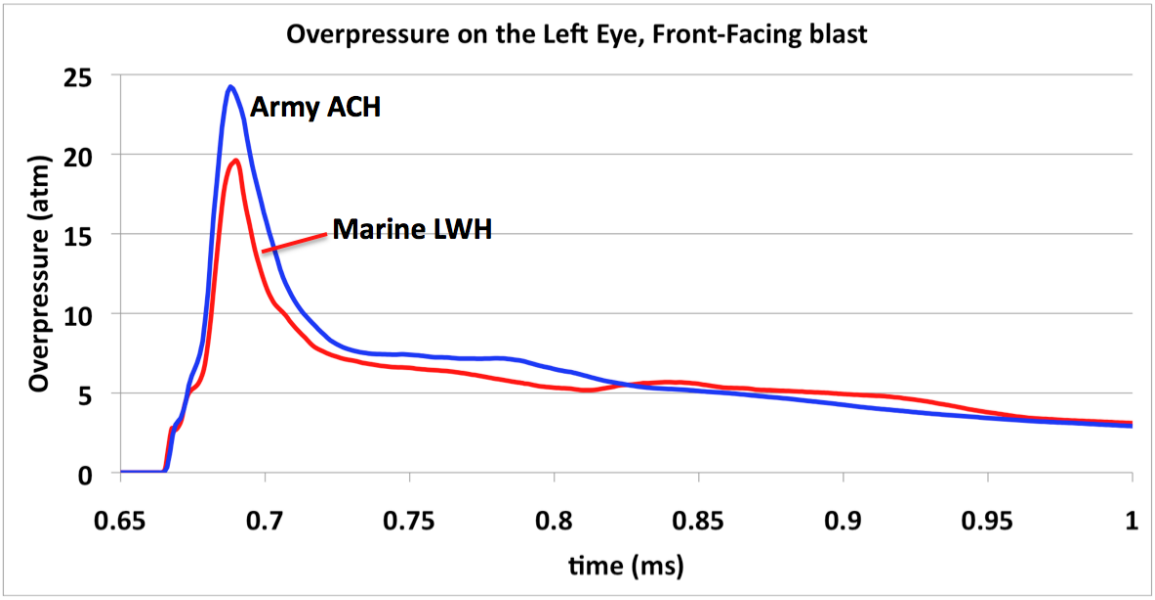

Figure 5.4 Overpressure history on the left eye (station 16) for the ACH and LWH due to a front-facing blast

5.3.2 Eye Pressure for the front-facing blast

For the front-facing blast, the LWH produces significantly lower peak pressures on the eyes than does the ACH due to the presence of the brim. Figure 5.4 shows the pressure histories on the left eye for the two helmets for this case, and Fig 5.5 shows snapshots of the pressure as the incident waves hit the two geometries. As the incident wave passes the front lip of the helmet, the wave is bent and turned by the geometry. Expanding around the corner to enter the gap between the helmet and head weakens the shock. In the LWH, this process starts sooner and is more pronounced than for the ACH due to the presence of the LWH's brim. As Fig 5.5 shows, the wave passing the LWH is altered by the expansion behind the brim. This expansion weakens the shock and, as Figure 4 shows, reduces the peak pressure applied to the eyes.

A critical observation at this point is that this pressure reduction on the eyes for the LWH is sensitive to the exact positioning of the helmet on the head. The fact that brim extends father from the head than the edge of the ACH provides a potential benefit for some blast scenarios, but the details of the location of the blast source and how the helmet is worn will greatly effect the resulting pressure field.

Figure 5.5 Pressure snapshots for the front-facing blast for the ACH (left) and LWH (right).

5.3.3 Station 44 (front-center) for the back-approaching blast

The most significant deviation between the LWH and ACH where the LWH pressure is higher occurs for the rear-oriented blast. Figure 7 shows the pressure histories for Sensor 44, located between the forehead and the crown of the head (see Fig 5.2). Both geometries show a double peak after 1

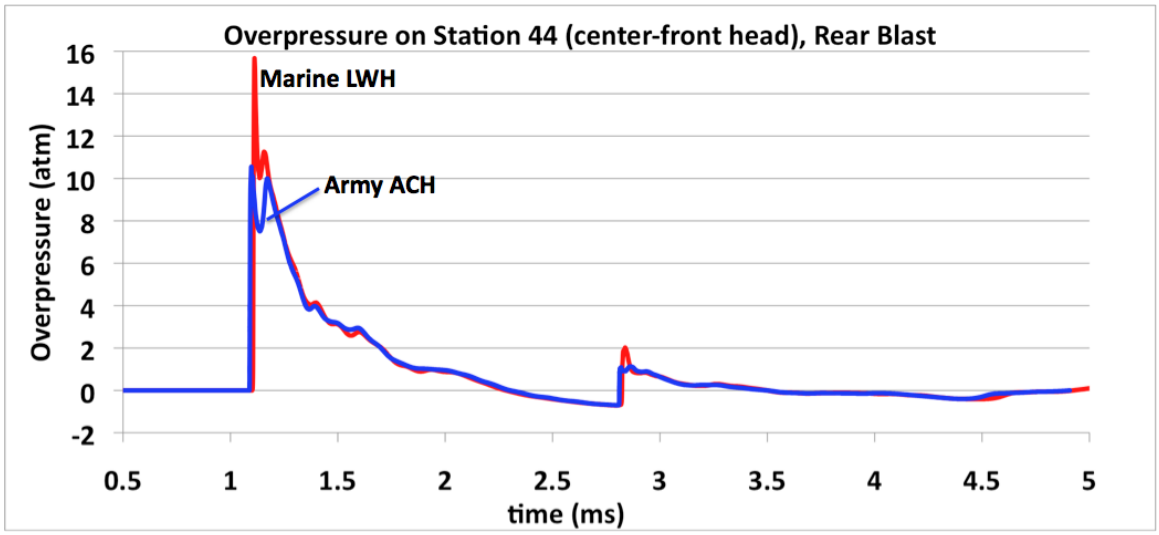

Figure 5.6 Pressure histories at station 44 (top-center forehead) for the Marine LWH and the Army ACH.

millisecond but the magnitude and spacing of these peaks differs for the two cases. The difference between these peaks is not an artifact of insufficient numerical resolution: the fall and rise between the

peaks in the ACH curve at 1.09 ms and 1.16 ms includes over 300 data points from the simulation. A secondary pressure increase is seen between 2.5 and 3 ms results from the ground bounce generated when the initial spherically-expanding wave produced by the explosive reflects from the ground. The difference in structure between the ACH and LWH pressures is seen again but on a more subdued scale.

For both helmet geometries, the penetrating waves from around the helmet perimeter meet near station 44. Figure 5.7 shows a centerline slice through these cases illustrating the pressure field during the wave propagation. Subtle differences between the two helmets influence whether the waves reach this point nearly simultaneously (for the LWH) or in a more staggered manner (as for the ACH). The black gap between the converging waves is larger for the ACH (Fig 5.7, top row) than it is for the LWH (bottom row) at the point when the first wave traverses the location of sensor 44 (denoted by the white circle and red arrow). The sensor is therefore detecting higher pressures near the wave confluence for the LWH.

Figure 5.7 Pressure contours showing wave convergence on the forehead for a back-approaching blast for the Army ACH (top) and Marine LWH (bottom). Red indicates absolute pressures above 7 atmospheres.

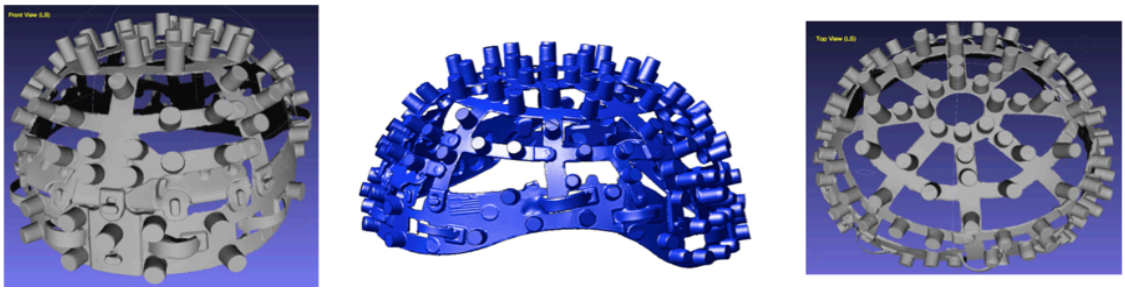

Figure 5.8 Surface scan of the post-based suspension of Schuberth. Left: front perspective. Middle: side view (front to left). Right: top perspective.

5.3.4 Post-based suspension

Simulations were also performed with both the ACH and LWH assuming a post-based suspension modeled after the Schubert design shown in Fig. 5.8.

Fig. 5.9 shows the implementation of this geometry for the blast simulations. An arrangement of ~130 rigid posts are placed under the helmet. These posts are of varying length to mimic the suspension design. Some posts are in contact with the helmet shell, while others are shorter and do not touch the helmet shell unless loading on the helmet results in displacement of the shell. The webbing that connects the posts is assumed to be flush with the skull and is not modeled in the current calculations. In the current study the geometry is assumed to be rigid.

Figure 5.10 shows an array of plots similar to Fig 3, but instead of comparing the ACH and LWH, Fig. 10 shows the difference between the ACH with no suspension and with the indicated post suspension. Analogous to Fig 3, 0 values indicate that the peak pressure at that location is the same in both cases. Data points above 0 indicate that the peak pressure for the open geometry is higher, and data points below 0 indicate that the peak pressure is higher at that location for the post suspension.

Figure 5.9 Post-based suspension as implemented in the Marine LWH. Posts with light-colored tips are in contact with the helmet shell. Left: front perspective. Middle: side view (front to left). Right: top

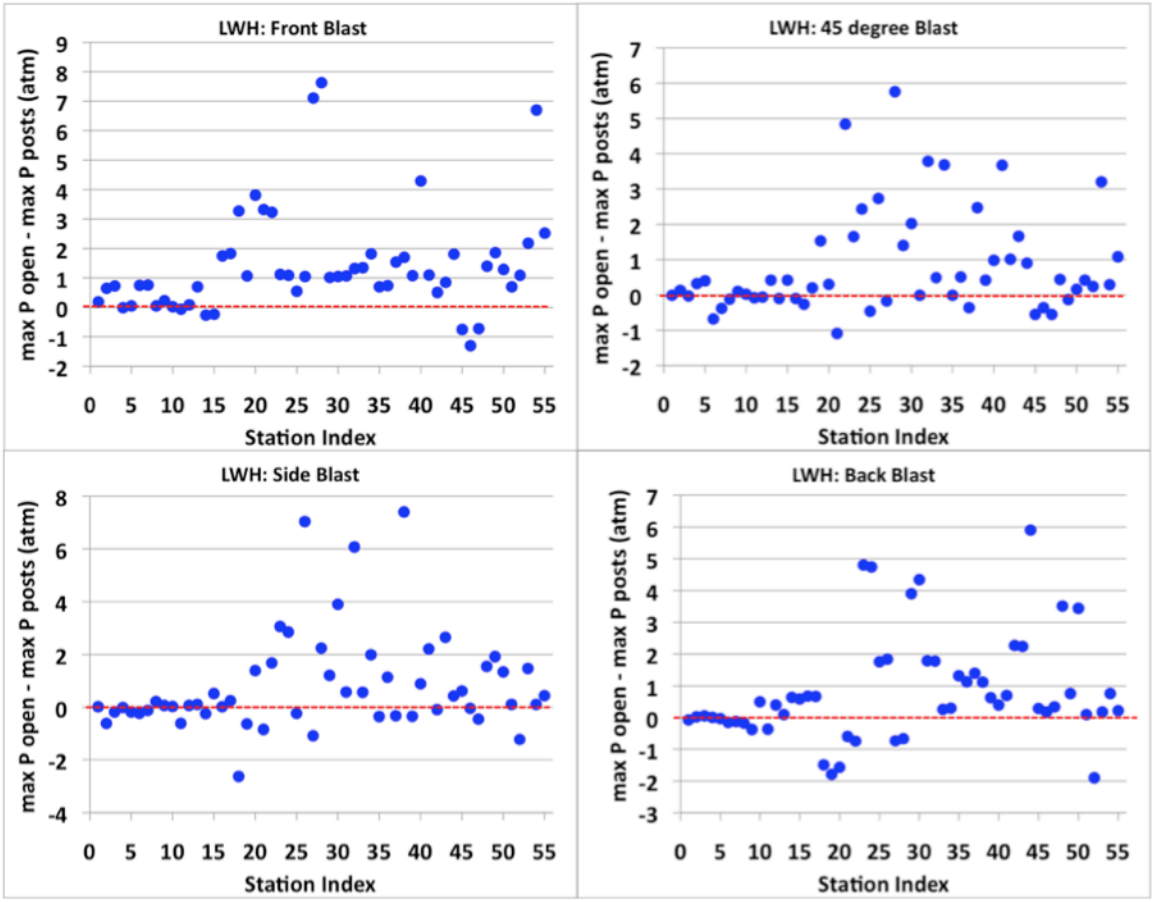

Figure 5.10 Difference in peak pressures between the open and post suspension systems at each sensor location and for four blast orientations. Values above 0: open geometry max pressure is higher; values below 0: max pressure for post geometry is higher

The presence of the posts tends to disrupt the wave propagation under the helmet, leading to generally lower peak pressures. Figure 5.11 gives one example of this effect for station 27 during a front-facing blast. This station is located approximately halfway up the rear of the head to the left side (see Fig. 2). Waves penetrating the gap between the helmet and head cause the initial pressure rise to approximately 2 atmospheres overpressure close to time 1 millisecond in Fig 5.11. This pressure increase is spread into two smaller jumps when the posts are present but the net pressure increase at this point is similar between the two cases. A much more significant pressure increase occurs between 1.1 and 1.2 milliseconds for the open geometry. This increase results from the waves focusing under the helmet on the rear of the head and generating a strong secondary wave that crosses the sensor location. This focusing mechanism is disrupted when the posts are present, producing a slower pressure rise and a much lower peak.

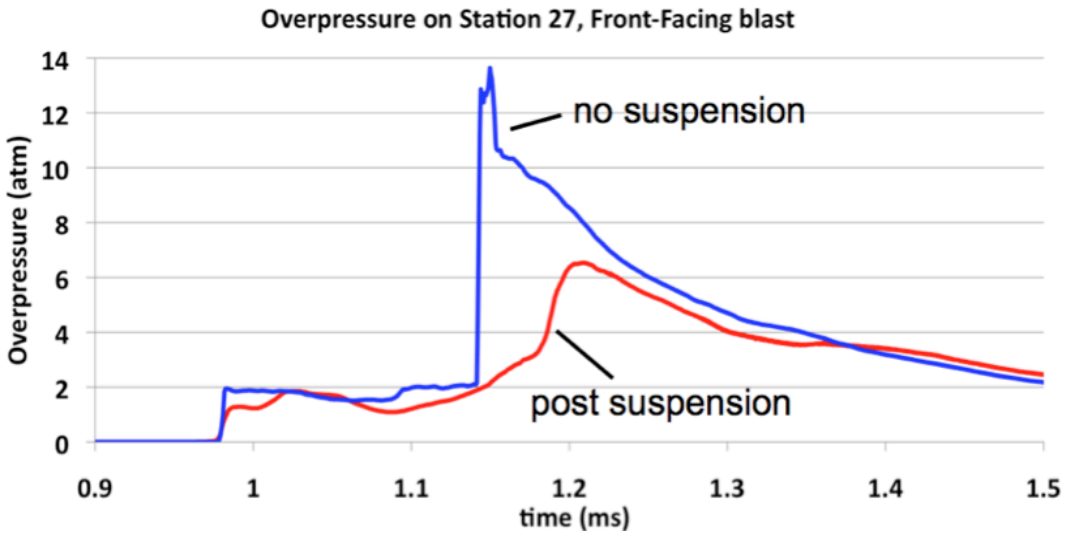

Figure 5.11 Overpressure at sensor location 27 for front-facing blast with (red) and without (blue) the post suspension geometry.

References

[5.1] C.R. Bass, K. Rafaels & R. Salazar, *Pulmonary Injury Risk Assessment for Short-Duration Blasts*, Proceedings from the Personnel Armour Systems Symposium PASS 2006, Leeds, U.K., September 18th-22nd, 2006

[5.2] D. R. Mott, D. A. Schwer, T. R. Young, Jr. J. Levine, J.–P. Dionne, A. Makris, G. Hubler, "Blast-Induced Pressure Fields Beneath a Military Helmet," Proceedings of the 20th International Symposium on Military Aspects of Blast and Shock, September 1st – 5th, 2008, Oslo, Norway.

5.4 Appendix: Peak Pressures for tested configurations.

Table 5.1: Peak overpressures in atmospheres at the stations in Fig 5.2 for the prescribed blast strength and source direction, for both helmet shell geometries and no suspension.

	Army ACH and Marine Corps LWH with no suspension.							
source:	front		quarter		side		back	
Station	ACH	LWH	ACH	LWH	ACH	LWH	ACH	LWH
1	9.80	9.79	6.28	6.28	3.16	3.18	1.56	1.57
2	10.95	10.93	6.42	6.43	3.69	3.69	1.96	1.97
3	14.28	14.26	6.41	6.40	5.12	5.10	1.73	1.74
4	7.58	7.64	7.87	7.87	5.25	5.26	2.47	2.51
5	18.38	18.55	9.93	9.92	3.23	3.29	2.15	2.17
6	16.45	16.56	14.68	14.30	4.45	4.37	2.47	2.46
7	15.16	15.14	11.21	11.18	8.18	7.96	2.67	2.66
8	1.90	1.90	1.59	1.57	3.36	3.58	7.67	7.63
9	2.01	2.23	1.55	1.66	3.38	3.49	8.29	8.20
10	2.29	2.29	1.57	1.74	3.73	3.87	11.80	11.78
11	2.49	2.53	1.87	1.87	4.40	4.03	13.49	13.46
12	2.84	3.28	2.07	1.99	4.49	4.79	11.13	11.14
13	5.72	6.58	2.03	2.41	3.12	3.23	7.73	7.05
14	3.67	3.93	6.64	5.23	6.58	4.40	2.93	2.80
15	3.70	4.03	4.21	4.22	3.52	3.60	2.87	2.86
16	24.24	19.60	19.39	15.36	6.73	5.72	3.86	3.04
17	24.22	19.81	8.17	6.83	2.04	2.07	3.92	3.04
18	5.32	6.66	4.41	4.54	2.61	2.97	2.56	2.37
19	9.89	10.10	5.57	5.73	3.40	4.07	2.46	1.91
20	4.68	7.12	4.88	5.71	3.13	4.80	2.77	2.34
21	7.72	8.00	4.15	3.86	2.74	3.53	2.33	2.33
22	7.53	8.00	11.32	10.15	3.64	4.97	2.31	2.24
23	4.61	4.64	3.33	5.35	6.23	6.82	8.14	8.30
24	4.72	4.61	4.45	5.97	6.67	6.36	8.15	8.28
25	4.85	4.07	3.39	2.94	4.03	3.06	4.03	4.76
26	5.28	4.52	8.58	8.63	9.99	12.77	4.28	4.97
27	13.06	13.64	3.80	4.03	2.81	2.96	2.54	2.28
28	12.10	14.28	10.50	11.76	4.03	5.61	2.29	2.40
29	4.26	5.10	4.52	5.18	4.25	4.44	9.24	10.30
30	4.32	5.25	6.71	6.53	9.05	9.03	8.95	10.66
31	5.16	5.28	2.83	3.57	2.74	3.50	4.22	4.63
32	4.59	5.73	8.58	10.61	13.35	13.47	4.04	4.77
33	7.92	8.81	3.16	4.05	2.95	3.36	2.76	2.88
34	7.75	8.82	10.12	11.95	4.25	6.00	2.55	2.89
35	4.32	4.98	3.77	3.70	3.15	3.10	6.85	7.18
36	4.28	5.14	5.76	5.91	6.21	6.75	7.00	6.95
37	5.14	6.03	3.03	3.77	2.84	3.44	4.04	4.63
38	4.68	6.39	8.01	9.67	18.54	16.42	3.76	4.58
39	6.80	7.23	3.65	4.13	3.28	3.31	3.10	3.45

40	14.00	12.46	5.59	6.06	3.80	4.18	3.85	3.68
41	6.31	7.32	13.58	15.34	6.48	8.62	2.82	3.54
42	4.60	5.25	4.93	4.96	3.89	3.33	7.89	9.18
43	4.62	5.64	8.20	7.55	5.33	7.64	8.08	9.23
44	5.52	6.73	5.79	5.71	4.08	4.31	10.55	15.66
45	6.68	5.27	6.49	6.74	5.92	5.84	4.53	4.22
46	4.83	5.06	4.72	4.89	3.32	3.26	5.16	6.23
47	6.71	5.39	3.89	4.16	2.57	2.66	4.51	4.34
48	4.35	4.84	4.04	3.19	4.92	4.50	7.09	6.74
49	4.84	5.26	4.12	3.24	4.28	5.93	7.07	6.67
50	4.59	4.73	4.46	3.71	4.99	5.34	7.16	6.71
51	5.72	6.58	2.03	2.41	3.12	3.23	7.73	7.05
52	9.15	10.21	5.18	4.47	3.16	3.49	2.78	2.22
53	8.67	9.48	7.91	7.41	3.86	4.18	1.99	2.23
54	12.24	13.31	5.91	6.59	3.97	3.89	2.17	3.01
55	12.12	10.28	5.08	6.07	3.24	3.77	3.05	3.13
56	5.98	6.78	5.75	6.87	4.30	4.82	4.33	4.79

Table 5.1 concluded.

Table 5.2: Peak overpressures in atmospheres at the stations in Fig 5.2 for the prescribed blast strength and direction of source, for both Army ACH and Marine Corps LWH, for the post-based suspension shown in Fig. 5.9. The location of Station 56 in the previous data places it inside a post, and therefore it is outside the flow field and not included.

Army ACH and Marine Corps LWH with post-based suspension.

source:	front		quarter		side		back	
Station	ACH	LWH	ACH	LWH	ACH	LWH	ACH	LWH
1	9.62	9.60	6.29	6.29	3.17	3.16	1.62	1.64
2	10.36	10.28	6.29	6.30	4.29	4.30	1.93	1.94
3	13.69	13.53	6.44	6.43	5.31	5.28	1.66	1.68
4	7.67	7.65	7.85	7.55	5.26	5.27	2.46	2.50
5	18.38	18.50	9.70	9.52	3.46	3.47	2.20	2.20
6	15.83	15.81	15.30	14.98	4.48	4.60	2.69	2.61
7	14.40	14.38	11.53	11.56	8.25	8.08	2.86	2.78
8	1.88	1.85	1.67	1.69	3.55	3.36	7.81	7.80
9	2.02	2.00	1.56	1.56	3.37	3.42	8.76	8.57
10	2.29	2.27	1.80	1.72	3.96	3.84	11.32	11.28
11	2.56	2.59	1.91	1.95	4.36	4.64	13.84	13.82
12	2.89	3.19	2.12	2.05	4.69	4.72	10.63	10.74
13	5.25	5.88	2.16	1.99	3.05	3.12	7.40	6.95
14	3.75	4.19	6.41	5.33	6.12	4.64	2.45	2.16
15	3.75	4.26	3.33	3.80	2.56	3.08	2.37	2.27
16	22.36	17.85	19.38	15.46	6.87	5.70	2.03	2.36
17	22.35	17.98	7.90	7.09	1.88	1.82	1.97	2.37
18	2.90	3.39	3.94	4.34	5.27	5.60	4.11	3.86
19	8.61	9.03	4.35	4.20	4.89	4.70	4.03	3.70

20	2.91	3.31	3.67	5.41	3.42	3.41	4.32	3.91
21	4.55	4.68	5.53	4.95	4.03	4.37	3.19	2.92
22	4.48	4.77	4.26	5.31	2.62	3.29	3.06	2.98
23	2.86	3.52	2.98	3.70	3.60	3.76	3.48	3.50
24	2.72	3.52	3.13	3.54	3.76	3.51	3.72	3.54
25	3.36	3.52	4.03	3.40	4.07	3.29	2.95	3.00
26	3.24	3.47	5.61	5.90	5.85	5.73	2.68	3.13
27	6.51	6.53	4.07	4.20	3.88	4.04	3.09	3.01
28	6.42	6.65	5.68	6.00	3.04	3.37	2.96	3.06
29	4.02	4.08	3.53	3.78	2.66	3.23	6.17	6.40
30	3.99	4.20	3.98	4.51	4.68	5.13	6.15	6.32
31	4.05	4.21	3.45	3.58	3.09	2.92	2.76	2.84
32	3.79	4.41	5.87	6.83	7.35	7.40	2.50	2.99
33	5.86	7.46	3.21	3.56	2.75	2.79	2.46	2.62
34	5.78	7.00	7.70	8.27	3.45	4.01	2.44	2.59
35	3.95	4.28	3.02	3.71	3.08	3.45	5.65	5.86
36	3.76	4.40	4.78	5.40	4.47	5.61	5.50	5.82
37	3.96	4.49	4.43	4.13	3.61	3.76	3.10	3.23
38	3.87	4.69	6.09	7.20	9.91	9.02	2.90	3.46
39	5.40	6.15	3.42	3.71	3.17	3.65	2.67	2.82
40	7.84	8.17	4.31	5.08	3.07	3.29	3.04	3.28
41	5.10	6.22	9.37	11.67	5.34	6.41	2.66	2.84
42	4.71	4.74	3.48	3.95	3.24	3.42	6.80	6.91
43	4.63	4.79	5.22	5.89	4.27	4.99	6.89	6.99
44	4.87	4.92	4.41	4.81	3.63	3.88	9.53	9.76
45	6.26	6.02	6.20	7.29	5.35	5.22	3.36	3.93
46	5.32	6.36	5.31	5.25	3.49	3.30	4.92	6.05
47	6.35	6.11	4.27	4.71	3.24	3.11	3.40	4.00
48	2.60	3.44	2.27	2.75	2.73	2.95	3.84	3.23
49	2.89	3.40	3.06	3.37	3.66	4.01	4.86	5.91
50	2.57	3.44	3.21	3.55	4.05	4.00	3.47	3.27
51	5.25	5.88	2.16	1.99	3.05	3.12	7.40	6.95
52	8.38	9.12	4.48	4.23	4.94	4.71	4.51	4.12
53	5.98	7.30	3.76	4.21	2.03	2.71	2.14	2.05
54	6.71	6.61	5.55	6.30	3.47	3.78	2.19	2.25
55	7.87	7.76	4.65	4.99	2.77	3.33	2.77	2.91

Table 5.2 concluded.

6. EFFECT OF CONFINEMENT BY ONE OR TWO WALLS

Blast Modeling Progress Report:
Effect of Confinement by One or Two Walls
Prepared for Marine Corps System Command – PM-ICE
In support of project: Infantry Combat Equipment Development and Evaluation
PI: Peter Matic, Naval Research Laboratory Code 6350

Authors: David Mott[1], Doug Schwer[1], and Theodore Young[2],
[1]*Code 6040, Naval Research Laboratory, Washington, DC*
[2]*Berkeley Research Associates, 6551 Mid Cities Ave, Beltsville, MD 20705*
January 7, 2013

6.1 Summary:

Computational studies of blast impingement on helmeted-head geometries including the upper torso have been performed to determine the effect of confinement of the blast wave by a nearby wall or corner. In each case a 1.5 KG C4 charge was placed three meters in front of the mannequin. In some cases these reflections from the walls arrived soon enough to interact with the ground bounce from the initial blast, increasing the intensity and complexity of the loading. In other cases, the reflections arrived after the ground bounce and effectively lengthened the time span of the loading while only moderately affecting the peak overpressures. The primary conclusions of the study include:

1. The highest pressures generated on the head were due to the initial wave from the blast hitting the unprotected areas of the face, specifically the eyes. Overpressure on the eyes peaked at approximately 7.5 atmospheres.
2. As the initial blast wave envelops the head and helmet, waves traverse each side of the face, over the top of the helmet, and penetrate the gap between the helmet shell and head. These waves intersect and generate a high pressure (~3.5 atm overpressure) on the back of the head.
3. Reflected waves from a single wall behind the mannequin are weaker than the incident wave. At 0.5 m stand off from the wall, these reflected waves arrive soon enough to interact with the ground bounce from the initial blast. Peak pressures on most of the head do not change, but peak overpressures on the back of the neck increase to approximately 2.5 atm for 0.5 m stand off.
4. The addition of a second wall forming a corner generates a much more complex wave interaction field and a higher potential for generating large amplitude reflected waves. Distinct reflections from the individual walls and from the wave interaction in the corner could be identified in the pressure histories.
5. Placing the mannequin 0.5m from both walls (symmetric case, Fig. 6.3) generated a large pressure spike on the neck of 5 atm that was not present in other tests but was in a location consistent with the increased neck pressure from the one-wall tests.
6. The asymmetric geometries (see Fig. 6.3) generated increased max pressures on one side of the back of the neck. Evidence of a strong wall-generated lambda shock (i.e., a stronger shock generated by the combination of the incident wave and a wall reflection) was not seen in the cases tested.

6.2 Mannequin Geometry and Computational Approach

Geometries of the Helmet Shell and Pad Suspension

Figure 6.1 shows the helmet, head, and torso geometry used in the calculations. The helmet shell is the Army Advanced Combat Helmet (ACH) and the liner is a set of Team Wendy pads. The ACH

geometry was provided by Natick Soldier Systems Center in the form of surface coordinates obtained by a three-dimensional scans of the inner surface and outer surface of the helmet. The inner and outer surfaces were combined to define the body used by the computational fluid dynamics calculation. Geometry of the Team Wendy pads was also provided by Natick Soldier Systems Center in the form of surface coordinates. The scans of the pads included only the surface of each pad that faces away from the helmet shell when installed. A model of each pad was then generated using analytical functions that reproduced the overall shape of each pad's surface but had the advantage of providing a simple, watertight discretization suitable for implementation within a fluid dynamics calculation. The detailed head, neck, and shoulder geometry was purchased from a commercial vendor [6.1], and the outline at the shoulders was extended down to form an approximate torso.

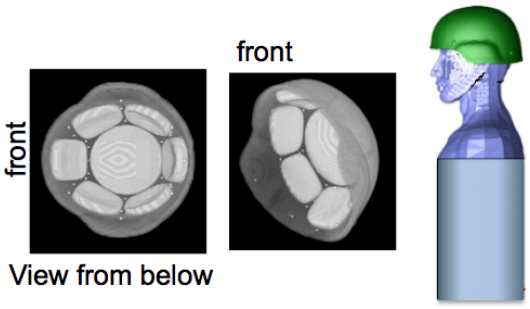

Figure 6.1: Helmet, head, and torso geometry.

In these calculations the geometry is assumed fixed and rigid, and the flow about the geometry and penetrating the gap between the helmet and shell is calculated. The computational approach included modeling the initial explosion using a reacting-flow simulation and then applying the resulting blast wave as boundary conditions for a detailed three-dimensional computation of the flow about the body. This approach has been described in detail elsewhere [6.2].

6.3 Single Wall and Corner Geometries

The source of the blast is a 1.5 kg C4 charge placed at face-level and three meters in front of the mannequin in all cases. This charge size and stand off distance corresponds to 99% survivability based on Bass's criteria for pulmonary injury [6.3]. Figure 6.2 shows a side view of the first three tested geometries: one with no wall (i.e., a free-field blast), and two with a single wall behind the mannequin. The stand off between the center of the mannequin and the wall is 1.0 and 0.5 meters in the two single-wall cases. Figure 6.3 shows a top view of three of the corner cases considered in this study. In these cases, the height of the mannequin and charge are the same as indicated in Fig. 6.2. The *normal* cases place the line between mannequin and charge at a 90° angle to one wall. The *asymmetric* cases place this line between charge and mannequin at 22.5° from this wall. Finally, the *symmetric* cases places this line between charge and mannequin at 45° from this wall. The stand off between the mannequin and the closest wall in the cases shown in Fig. 3 is 1 meter, and comparable cases were studied with this spacing reduced to 0.5 meter.

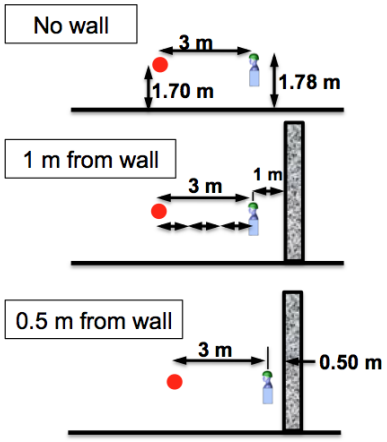

Figure 6.2: Single-wall geometries

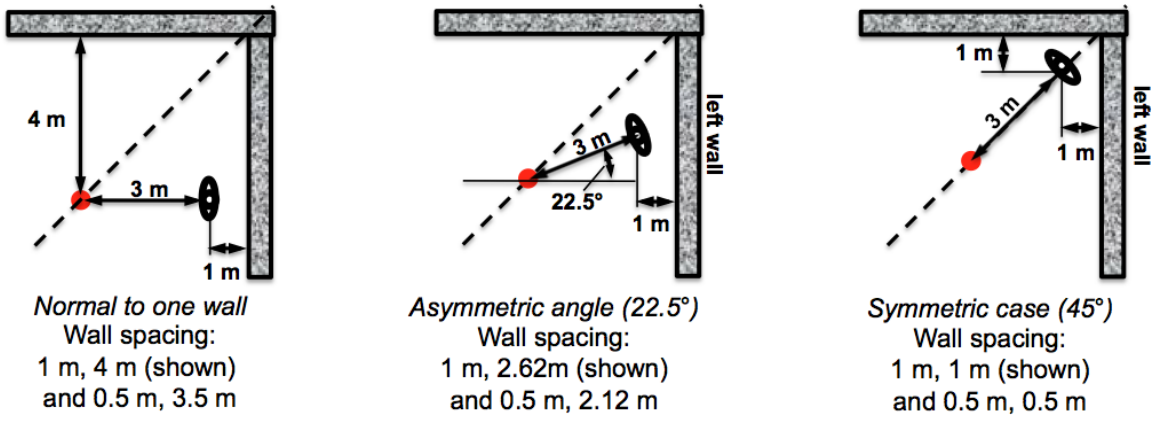

Figure 6.3: Corner geometries (top views).

Results of initial exploratory calculations demonstrated that for the geometries under consideration, the normal cases were not significantly different from the comparable single-wall cases, so those results will not be shown. For the normal cases, reflections from the second, more distant wall were weak compared to the initial blast wave and reflections from the closer wall.

6.4 Results

The following sections describe the distributions of pressure on the head beneath the helmet, the maximum pressure at each location on the head, and representative time histories for important locations on the head and neck. The helmet shell and pads are present in all simulations but are not shown in the following figures so that the pressure on the head beneath the helmet is visible.

6.4.1 Free-field

Figure 4 shows an array of pressure distributions for various times after the blast arrives in the free-field test. The incident wave paints the entire face with elevated pressures and generates high peak pressures on the eyes. A reflection of this wave from the forehead pad generates an elevated pressure on the forehead seen at 0.00071 s. As the incident wave envelops the geometry, a reflection from the chest washes up over the face

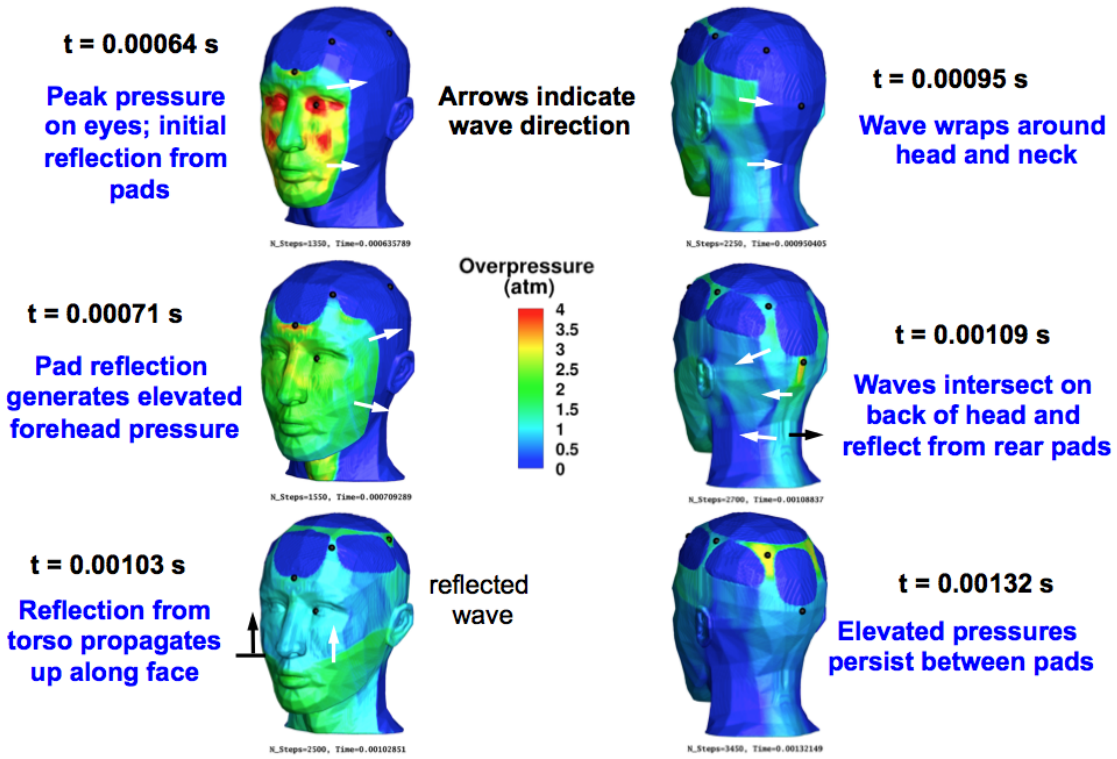

Figure 6.4: Pressure evolution for no wall

(0.00103 s). Waves from left and right intersect behind the head and neck to generate an overpressure in excess of 3 atmospheres.

Figure 6.5 shows the peak pressure distribution for the free-field configuration as well as pressure histories at selected locations. The initial blast wave generates the peaks seen before 0.002 s. The ground bounce and secondary shock generated by a spherical charge generate the cluster of peaks seen after 0.003 s. An overpressure of 7 atm is generated on the eyes when the initial blast wave reflects from the face. This is the highest overpressure on the head during the simulation. Peaks of approximately 3 atm are seen on the back of the head where waves interact with each other and reflect from the pad surfaces.

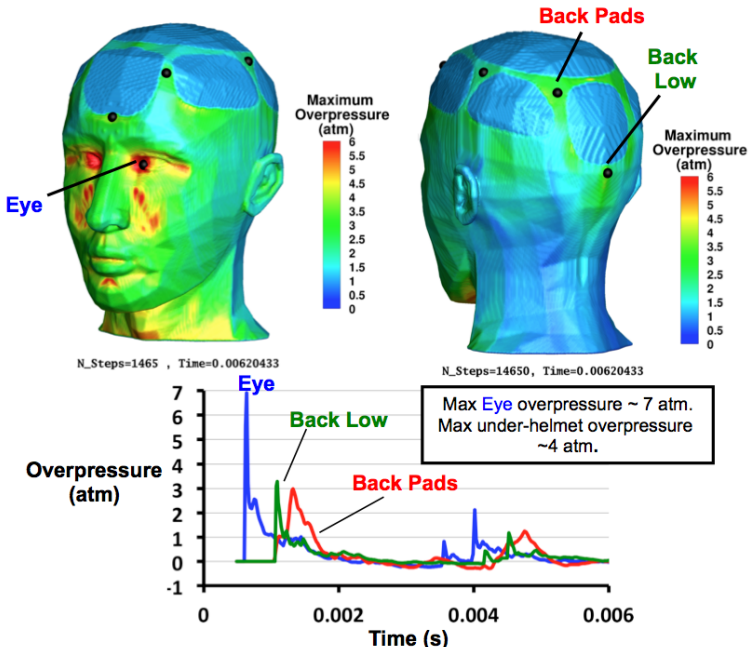

Figure 6.5: Max overpressure and selected overpressure histories for no wall

Since the incident wave is identical for the various cases tested, the pressure histories on the head are identical up until the point when reflected waves affect the flow field near the head. In order to focus on how the walls change the results, most plots in the following sections will start at 0.002 s, which is after this common response to the initial wave. The time required for the wall reflections to reach the model depends on the stand off and orientation, so the range of time plotted for the pressure histories varies between cases.

6.4.2 Single-Wall

Figures 6.6 through 6.9 show the effect of adding a single wall behind the mannequin. Figure 6 shows the modest effect on the pressure histories when this wall is placed 1 m behind the mannequin. Additional loading is seen on the back of the head after 0.0005 s due to reflections from the wall, but this loading is modest and comes after the arrival of the ground-bounce waves. A modest increase in the max pressure on the neck is also seen when comparing the distributions in Fig. 6.6 to Fig. 6.5. Figure 6.7 shows the evolution of surface pressure when the wall is placed 0.5 m behind the mannequin. The wave reflected from the wall reaches the back of the head at approximately 0.0028 s, which is significantly sooner than the arrival of the ground bounce from the front. Figure 6.8 shows that this overpressure on the back of the head plateaus below 1 atm overpressure around 0.003 s and then generates a rounded peak of about 1.3 atm. Figure 6.9 highlights the comparison between the no-wall case and the one-wall case. Identical response is seen on the back of the head for the initial wave. Reflections from the wall generate a broad loading (shown in the orange and blue curves) between 0.002 s and 0.004 s. The reflected waves also elevate the peak pressure experienced by he back of the neck, as shown by the distributions in Fig. 6.9. The peak overpressure in this area reaches approximately 2.5 atms.

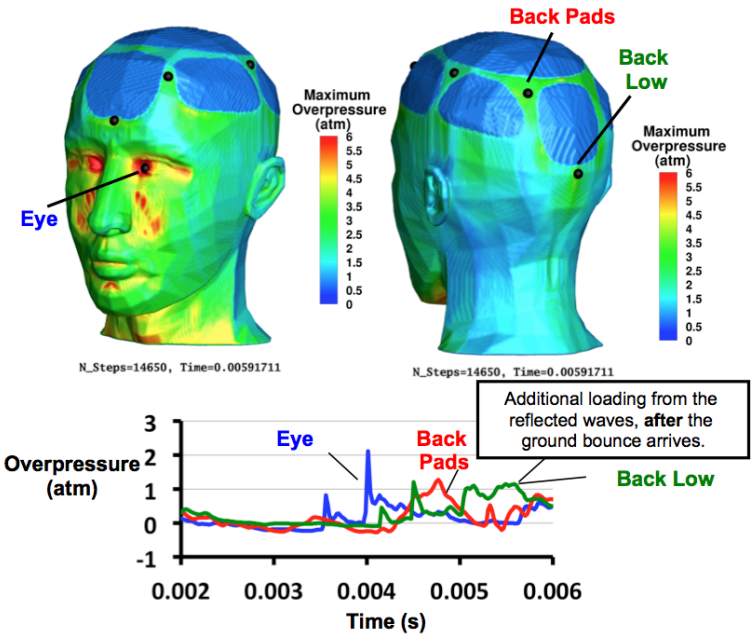

Figure 6.6: Max overpressure pressure and selected overpressure histories for one wall, 1 m behind

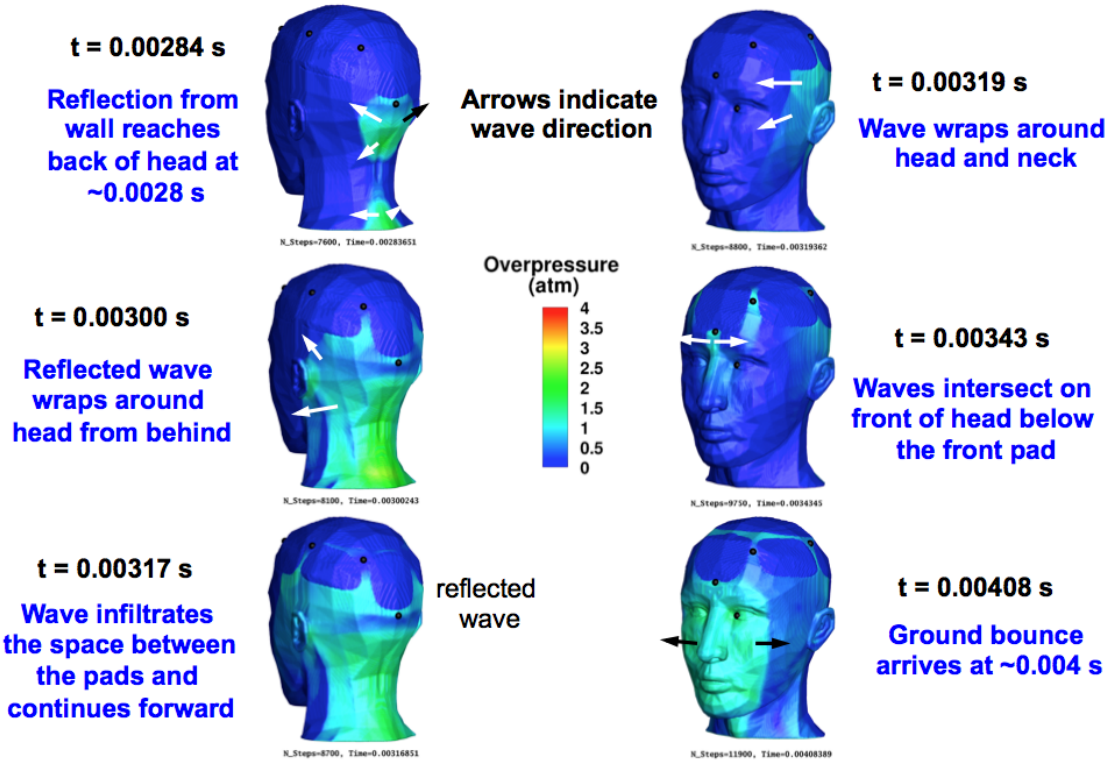

Figure 6.7: Pressure evolution for one wall at 0.5 m behind mannequin.

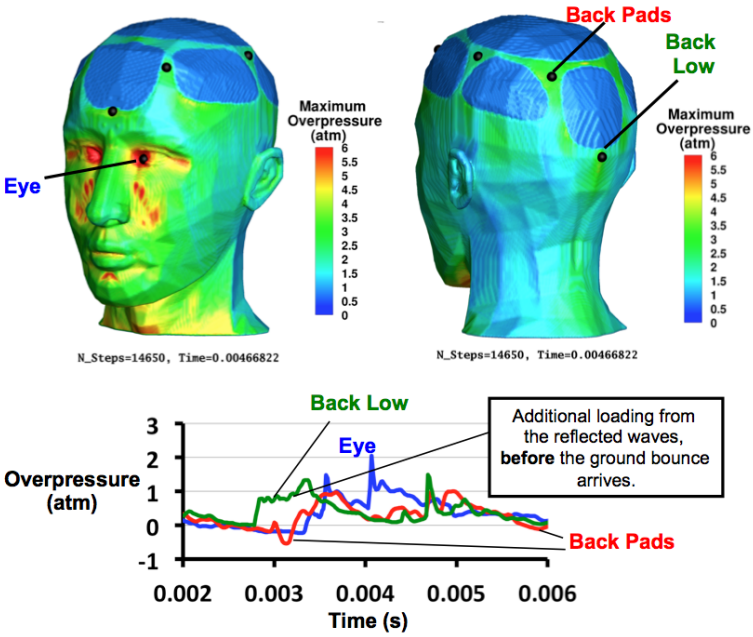

Figure 6.8: Max overpressure distribution and selected time histories for one wall at 0.5 m

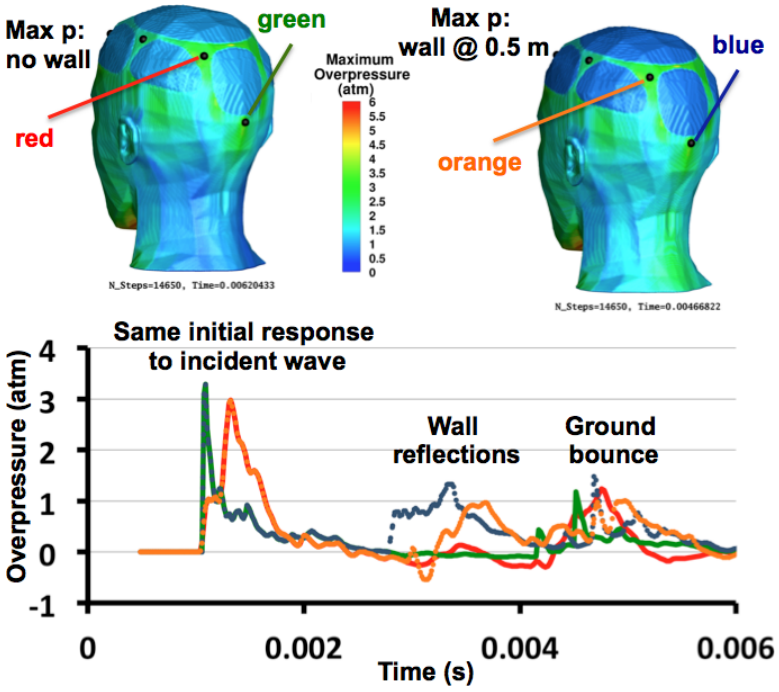

Figure 6.9: Comparing no wall and single wall at 0.5 m.

6.4.3 Symmetric Corner Cases

Figure 6.10 shows the pressure evolution for the symmetric corner case with 1 m stand off. This stand-off is large enough that the ground bounce arrives prior to the reflections from the walls. The wall reflections occur in two distinct phases. The first is the direct reflections from the left and right walls that intersect the sides of the head close to each ear (0.0038 s). Figure 6.10 focuses on the left-rear of the head, but the same pattern appears on the right-rear of the head as well. These waves wrap around the head and interact in a relatively weak way. A stronger reflection is seen centered on the back of the head and neck at approximately 0.0065 s. This reflection is generated by the incident wave and reflected waves interacting in the corner behind the mannequin; the symmetric nature of the geometry then results in a wave returning from the corner that is centered on the back of the head.

Figure 6.11 shows that the reflected waves from the walls in this case interact with the ground bounce to generate elevated pressures on the back of the head, but, as in the previous cases, the peak values (this time in the range of 2 atm overpressure) are still lower than the peaks generated by the initial waves wrapping around the head from the front. The reflection from the corner provides a late, weak elevation in the pressure.

Figure 6.12 shows the pressure evolution for the symmetric corner case with 0.5 m stand off. The closer proximity to the wall generates a stronger reflection that strikes the sides of the head behind the ears at approximately 0.0023 s. These reflected waves arriving from the left and right walls intersect at the back of the head and generate a region of high-pressure on the lower head and upper neck (0.00234 s). These waves continue to wrap around the head and intersect again on the face. The reflection from the corner arrives at the back of the head at approximately 0.00350 s. This wave envelops the head from the rear and generates elevated pressures on the face as the waves interact.

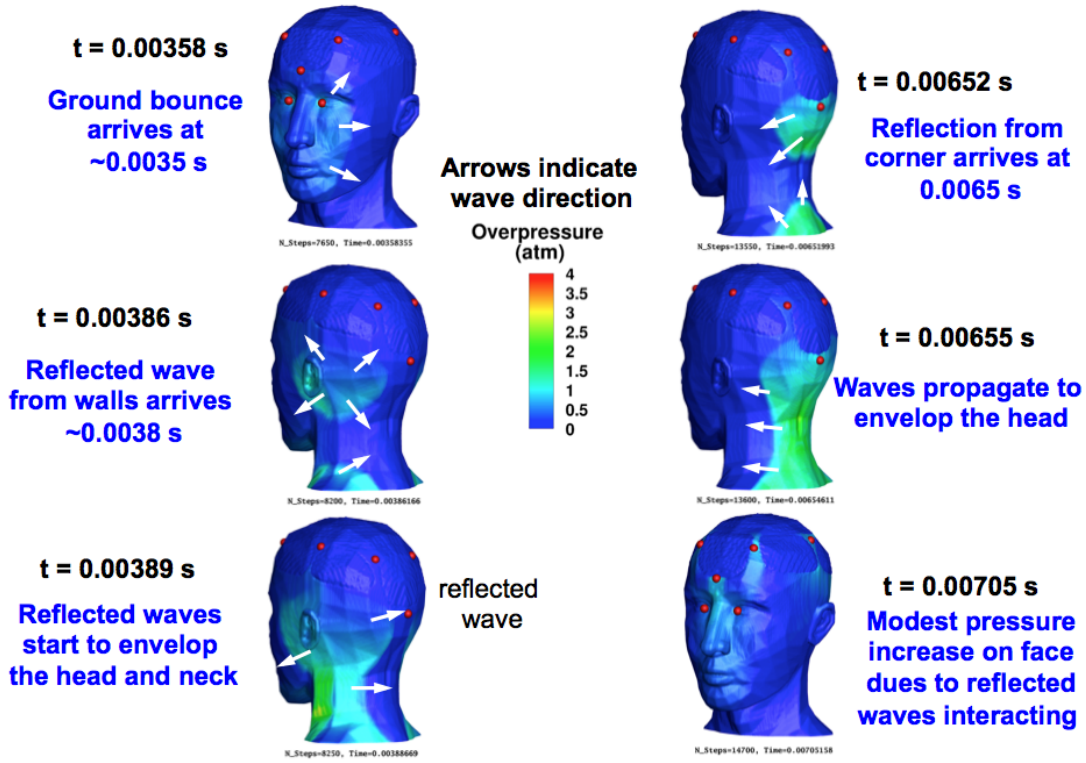

Figure 6.10: Pressure evolution for symmetric corner placement at 1 m stand off

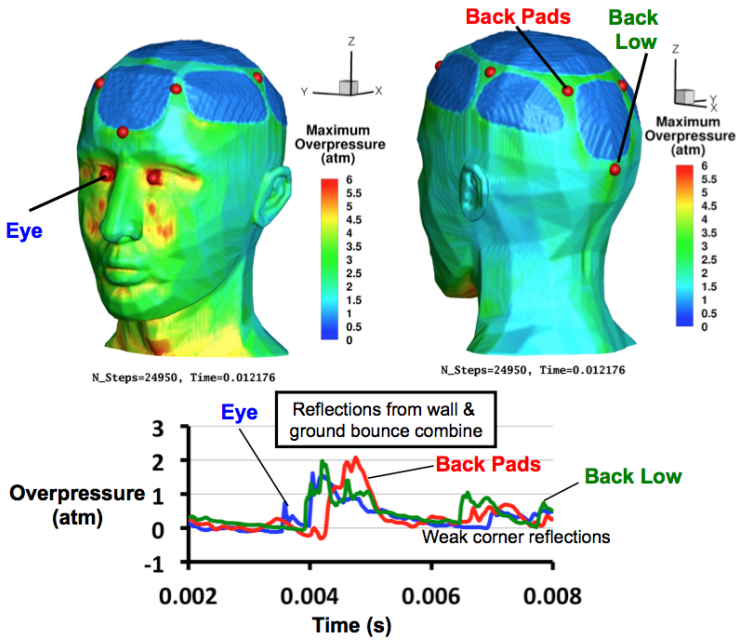

Figure 6.11: Max overpressure and selected histories for the symmetric case at 1 m.

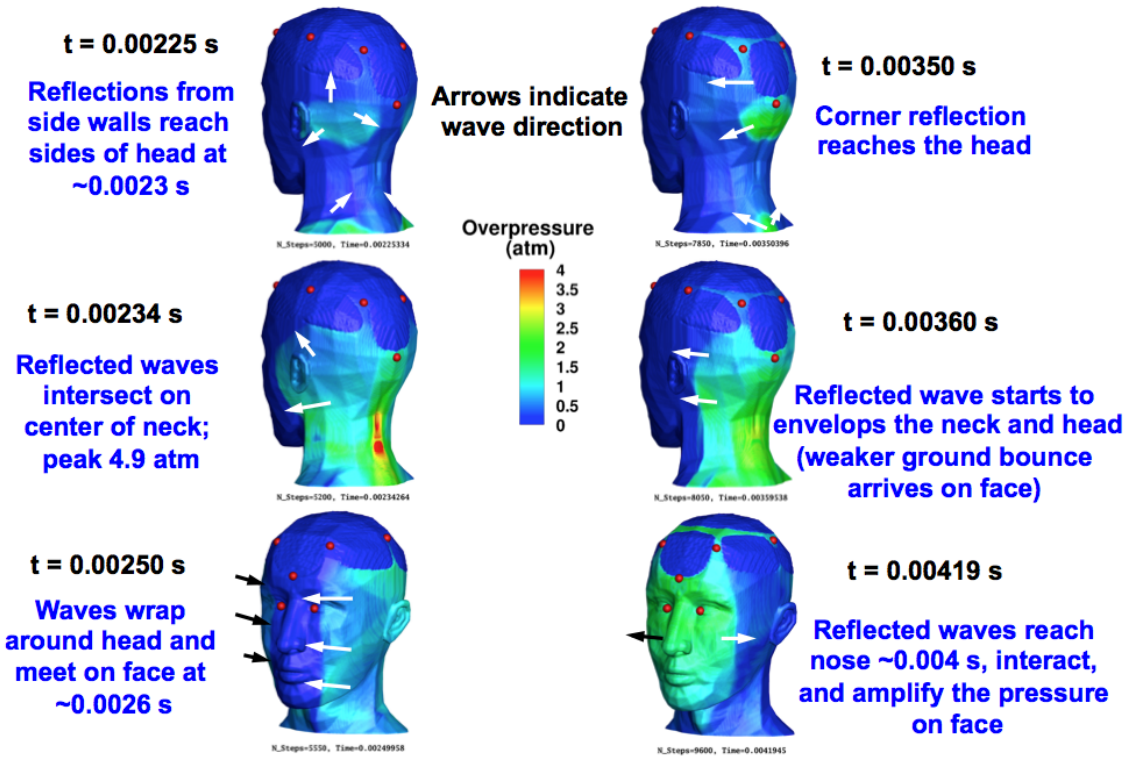

Figure 6.12: Pressure evolution for the symmetric corner case at 0.5 m.

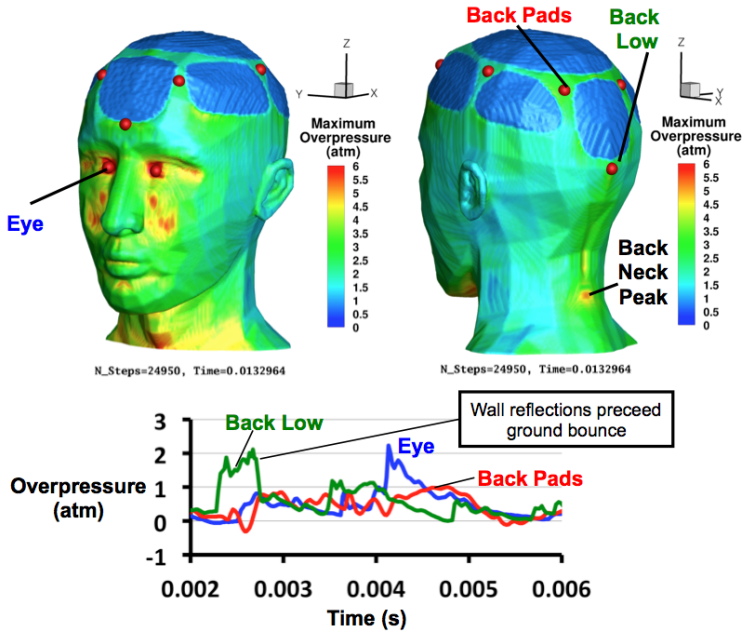

Figure 6.13: Max overpressure and histories at selected locations for the symmetric case at 0.5 m.

Figure 6.13 shows that the maximum pressure distribution on the front of the head is largely unchanged compared to the previous cases, but the back of head and neck sees a higher and broader maximum

pressure. The wall reflections arrive much earlier than the ground bounce and are significantly stronger than in the previous cases (peaking at more than 2 atm overpressure).

Figure 6.13 also identifies a new point of interest on the neck labeled "Back Neck Peak," and Fig. 6.14 shows the pressure histories at this location compared to the "Back Low" location, which is just below the rear helmet pad. Fig. 6.13 starts at time 0 and shows that the peak due to the initial blast wave (occurring at just after 0.001 s) is significantly weaker at the lower location compared to the location near the pad. However, both the side-wall reflections and later corner reflections amplify the pressure at this point more significantly. The initial waves enveloping the head from the front wrap the back of the head and around and combine constructively near this top pad, and the pressure is also amplified by wave reflection from the pad. For the reflected waves from the walls, the strongest interaction is lower on the neck where the two waves collide nearly "head-on." For the corner reflection, the lower location receives a direct hit from the wave, whereas the back of the helmet protects the higher point near the pad. The wave must refract around the helmet and travel up to this higher point, which weakens the wave and leads to a lower peak at the higher location.

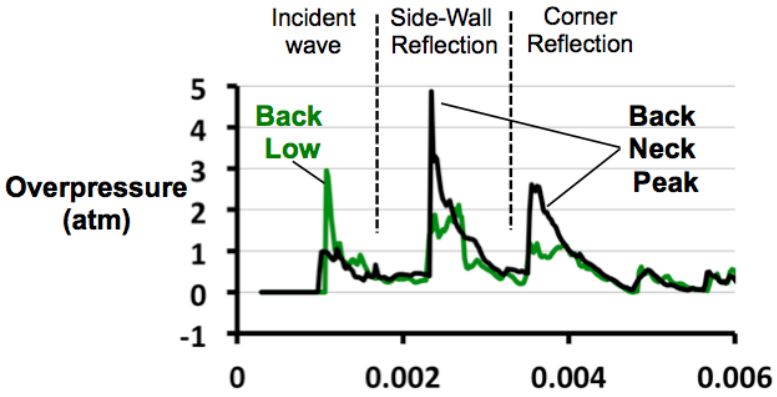

Figure 6.14 Overpressure at "back-low" and "back-neck-peak" locations for symmetric case at 0.5 m stand off from wall.

6.4.4 Axisymmetric Corner Cases

Figure 6.15 shows the pressure evolution for the asymmetric case with stand off of 1 m from the closest (left) wall. The stand off is sufficiently high for the ground bounce to arrive (~0.0035 s) before the reflection from the close wall. The reflection strikes the back-left side of the head and envelops the geometry. After wrapping around the head, the reflected waves penetrate the gap between the helmet shell and the head and interact on the front right of the head (0.00525 s), but the pressures produced are relatively weak. The same wave dynamics repeat after 0.008 seconds when the (considerably weaker) wall reflection of the ground bounce reaches the head.

Figure 6.16 shows the maximum pressures and pressure histories at selected points for the 1-m asymmetric case. The asymmetry is seen in the maximum pressure plot: viewed from the rear, the left side of the neck shows 1 to 2 atm higher overpressure compared to the right side of the neck. The histories plotted in Fig. 6.16 show complicated wave interactions between 0.004 and 0.006 seconds as the ground bounce interacts with the wall reflections from the initial wave. The wall reflections of the ground bounce arrive between 0.008 and 0.01 s and are relatively weak. Beyond 0.01 s, reflections from the distant corner reach the head but are weaker still.

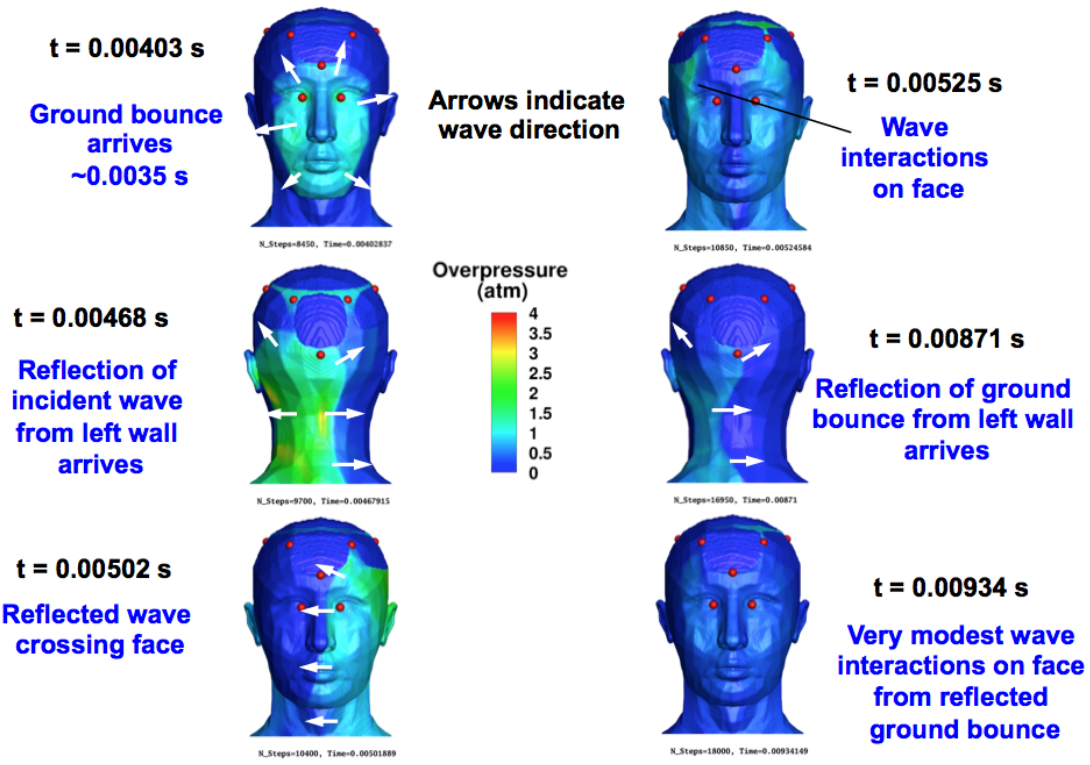

Figure 6.15: Pressure evolution for the axisymmetric case at 1.0 m stand off from wall.

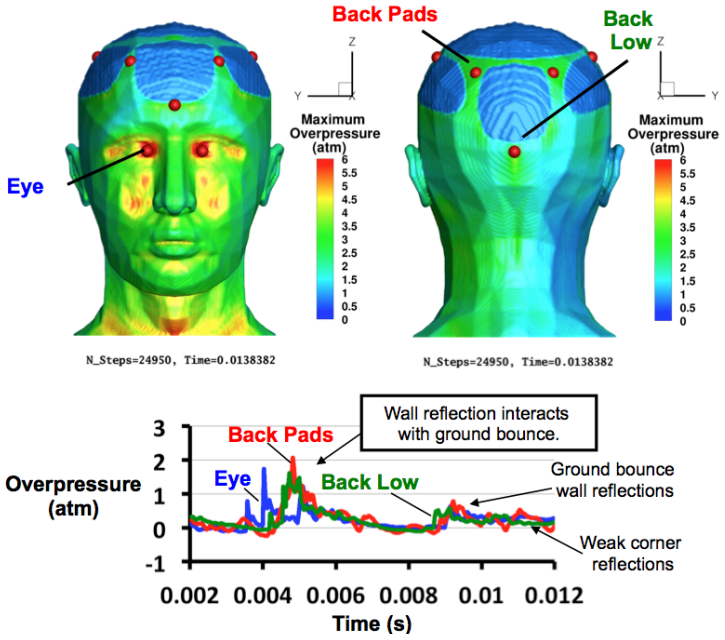

Figure 6.16: Max overpressure and selected histories for the asymmetric case at 1.0 m.

Figure 6.17 shows the evolution of pressure for the last case: the asymmetric corner geometry with 0.5 m stand off from the closest wall. Due to the closer stand off, the reflection from the wall reaches the

geometry before the ground bounce. As in the previous case, the reflected wave first strikes the back of the head on the left side. The wave envelops the geometry and the waves interact on the right side of the face. The ground bounce arrives at approximately 0.0026 s. The reflection of the initial wave, traveling from the mannequin's left to right, alters the propagation of the ground bounce, skewing its direction and making it hit the face off-center and to the mannequin's right. The reflection of the ground bounce from the wall arrives at approximately 0.0065 s and a similar wave propagation pattern is seen as in the initial reflected wave but with significantly lower pressures.

Figure 6.18 shows a similar asymmetric pattern to the peak pressure on the neck, similar to the results in Fig. 6.16. The closer proximity to the wall does make the reflected waves stronger than in the previous case with 1 m stand off, but the comparison is complicated by the wave interaction with the ground bounce. In the 1 m asymmetric case, the ground bounce elevates the pressure about the head and interacts with the reflected wave, producing higher pressures than the reflected wave would have generated on its own. For the specific charge placement and size tested, the maximum pressure distribution is very similar for 0.5 m and 1.0 m stand off.

Finally, Fig. 6.19 combines the overpressure traces for the back-low location for all four of the corner cases. The range of Fig. 6.19 captures effects of the initial blast wave and the reflection from the closest wall (for the asymmetric cases) or both walls (for the symmetric cases). The symmetric case with 0.5 m stand off shows the quickest increase in loading, and this loading is significantly higher than the other cases. The 0.5 m asymmetric case shows a broad reflection similar to the 0.5 m symmetric case but with a lower amplitude. The 1-m symmetric case shows a much later pressure rise due to the reflected waves, but the pressure increase is relatively broad as the reflected waves interact with the incoming ground bounce.

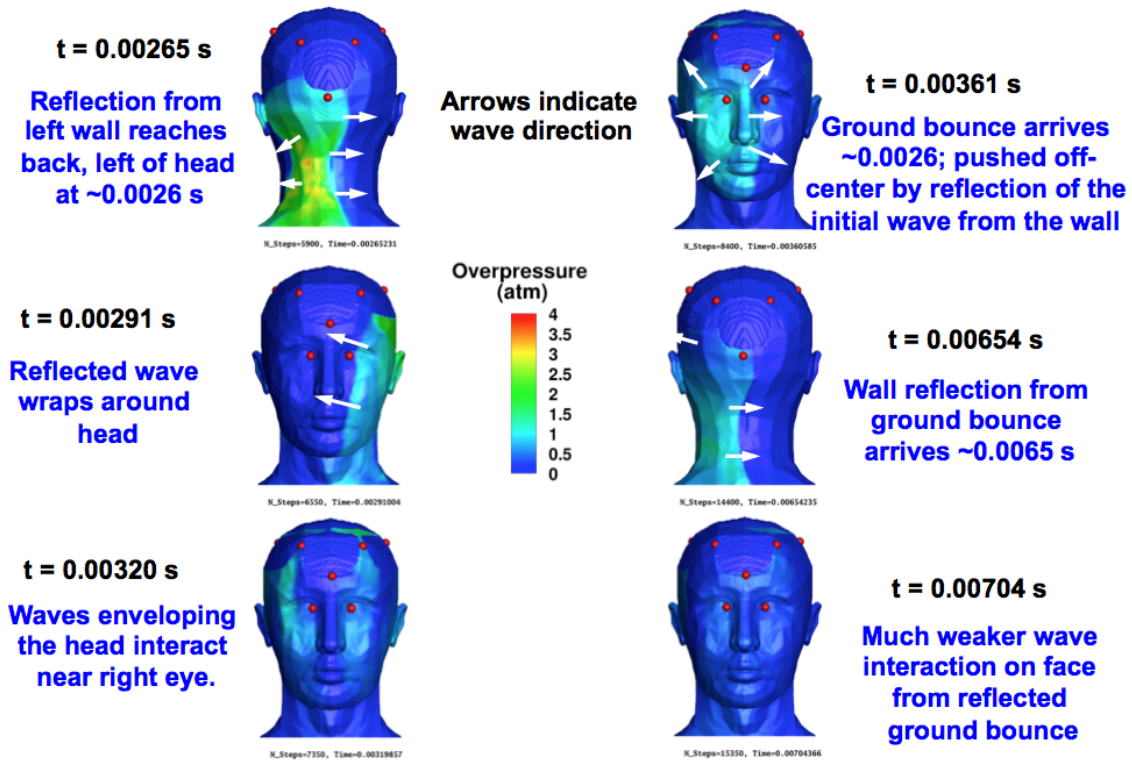

Figure 6.17: Pressure evolution for the asymmetric case with 0.5 m stand off from near wall.

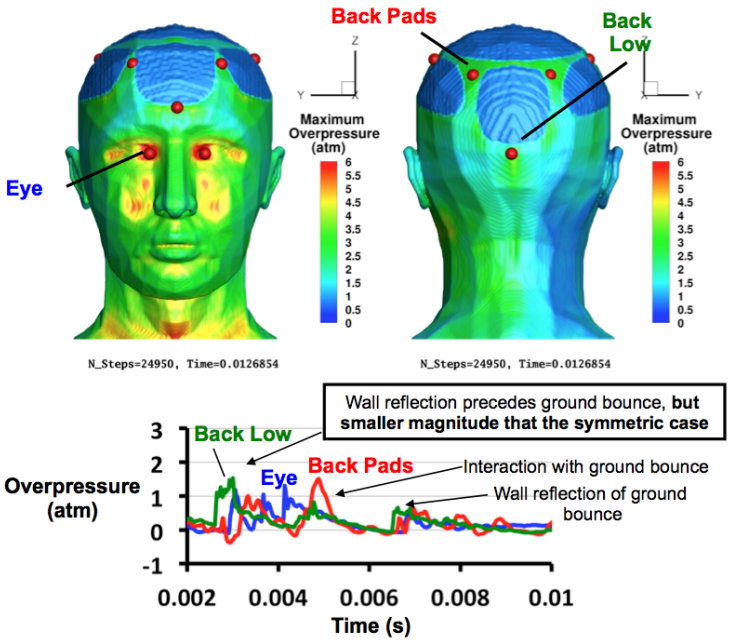

Figure 6.18: Max overpressure and histories at select locations for the asymmetric case with 0.5 m stand off from the nearest (left) wall.

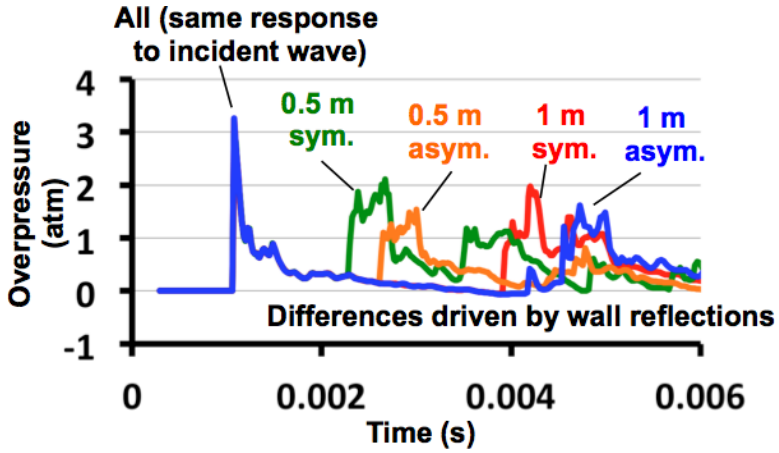

Figure 6.19: Pressure histories for the "back-low" location for the four different corner scenarios.

6.5 Conclusions

Computational studies of blast impingement on helmeted-head geometries including the upper torso were performed to determine the effect of confinement of the blast wave by a nearby wall or corner. In considering peak pressures generated on the head and torso, the presence of walls and corner geometries have the greatest effect on peak pressures when (a) the walls are close, so as to provide stronger reflected

shocks, and (b) waves from the reflections and from the incoming blast interact with each other (i.e., collide) at or near the head geometry. On the head, the peaks from the reflected waves are typically lower than the peak generated by the initial wave (for the locations studied), but these reflected peaks are also broader and more complex. On the back of the neck, the reflected waves did generate pressures that were significantly higher (particularly for the 0.5 m stand off) than the peak pressure generated on the neck without a wall.

REFERENCES

[6.1] TurboSquid, http://www.turbosquid.com/.
[6.2] Mott, D. R., Schwer, D. A, Young, T. R., Jr., Levine, J., Dionne, J.–P., Makris, A., Hubler, G., 2008. "Blast-Induced Pressure Fields Beneath a Military Helmet," Proceedings of the 20th International Symposium on Military Aspects of Blast and Shock, September 1st – 5th, Oslo, Norway.
[6.3] Bass, C.R., Rafaels, K. and Salazar, R., 2006. *Pulmonary Injury Risk Assessment for Short-Duration Blasts*, Proceedings from the Personnel Armour Systems Symposium PASS 2006, Leeds, U.K., September 18th -22nd.

7. APPENDIX: MABS 2008 MANUSCRIPT

The following article was presented at the 20th Military Aspects of Blast and Shock (MABS) Symposium in Oslo, Norway, 1-5 September 2008. The citation for the work is:

Mott, D. R., Schwer, D. A, Young, T. R., Jr., Levine, J., Dionne, J.–P., Makris, A., Hubler, G., 2008. "Blast-Induced Pressure Fields Beneath a Military Helmet," *Proceedings of the 20th International Symposium on Military Aspects of Blast and Shock*, September 1st – 5th, Oslo, Norway.

BLAST-INDUCED PRESSURE FIELDS BENEATH A MILITARY HELMET

David R. Mott[1], Douglas A. Schwer[1], Theodore R. Young, Jr.[1]
Jeffrey Levine[2], Jean-Philippe Dionne[2], Aris Makris[2], Graham Hubler[1]

[1]*Naval Research Laboratory, Washington DC*
4555 Overlook Ave SW, Washington, DC 20375
[2]*Allen-Vanguard Corporation (Med-Eng Systems)*
2400 St.Laurent Blvd., Ottawa, Ontario, K1G 6C4 Canada

ABSTRACT

The pressure field surrounding a head with a helmet subjected to a blast wave typical of injurious but non-lethal threats was investigated by coordinated experiments and numerical simulations. Experiments were conducted with C4 explosive charges ranging from 0.75 kg to 5 kg, and two anthropomorphic test mannequins (Hybrid III) located 3 m from the explosive. Experimental diagnostics included pressure sensors mounted at selected locations around each mannequin's head and in the free-field. Numerical modeling was done using a two-step approach. First, the blast and ground reflection were computed using a multi-component, reacting flow model. Second, the results were used to specify the boundary conditions for a three-dimensional unsteady simulation of the head-helmet complex subjected to a blast wave. Experiments and simulation results were verified and found to be consistent with one another. Results showed that the highest pressures developed when the mannequin faced 45º from the explosive charge. Pressure waves that entered the gap between the helmet and head focused on the side of the head away from the blast. The helmet also was shown to provide protection against primary blast injury both in computations and experiments.

INTRODUCTION

A high incidence of blast-induced Traumatic Brain Injury (TBI) has been diagnosed in soldiers fighting in the current conflicts in the Middle East. This injury describes various levels of brain function impairment, which follows exposure to blasts mostly from Improvised Explosive Devices – IEDs [1, 2].

Causes for blast-induced head injuries are not well understood. Blast-induced TBI can result from high-velocity fragments hitting the head (secondary blast injury), from the head impacting rigid surfaces after the body has been propelled by the blast, and from the brain impacting the bony structures from the skull following the blast (tertiary blast injuries). In the automotive field, where "tertiary-type" injuries are observed, head acceleration as measured in the skull of anthropomorphic mannequins is commonly used as a surrogate for brain injury. The Head Injury Criterion (HIC), developed by Versace [3], relates head linear-acceleration to observed severity of brain injury (Prasad, Mertz [4]). The HIC methodology has been extended to blast scenarios [5], but the appropriate filtering frequency to be used to make sure that the high-frequency blast related events are appropriately captured is not yet well defined [6].

There is also a question of whether brain injuries can result from direct exposure to the blast (primary blast injury). In particular, researchers have pointed out the possibility that brain injuries could result from overpressure in the torso, which causes physiological processes that might lead to TBI [7-9]. Although no head-injury criteria currently exists related to pressure measurements on the head (other than ear-overpressure injury [10]), high pressures that develop underneath combat helmets are likely to cause severe injury.

This present paper focuses on the direct effects of overpressure (primary blast). The pressure field around the head of a soldier wearing a combat helmet exposed to a representative blast is investigated both experimentally and numerically. Results of experiments using anthropomorphic mannequins wearing combat helmets are used to lay out the foundations necessary for correlating pressure measurements with TBI. Three-dimensional unsteady numerical simulations are used to describe and explain the pressure and flow-field around the head and helmet of a soldier exposed to a blast wave. Finally, comparisons between the experimental and numerical results are used to validate both methods for further studies and add insight into the physics.

EXPERIMENTAL METHOD

Tests in this trial series were conducted in Area P of the Canadian Forces Base (CFB) Petawawa, outside Pembroke, Ontario, Canada. Two automotive crash test mannequins (Hybrid III), which are representative of a 50th percentile North American male subject (full mannequin height: 1.75 m, 5'9", mass: 77 kg, 170 lbs), were subjected to blasts from high explosives. Two mannequins were employed to maximize the amount of data that can be obtained from each blast. Prior to testing, the legs and lower torso of each mannequin were removed. The upper torso and head of the mannequins were mounted on a specially designed positioning rig. These rigs allow the mannequins to react appropriately due to the initial blast wave while standing up, free of additional positioning rigs. This mimics the mannequin rigging methodology used by University of Virginia's Center for Applied Biomechanics [6].

In each trial, the mannequins were placed at 90º from one another, with a cylindrical C4 charge placed upon a cardboard Sonotube to provide the required height of burst. Figure 1 provides photos of the two mannequins, pressure sensor and charge configurations. The mannequins were placed in four different orientations with respect to the blast during the trial series: front, 45º, side, and back.

Figure 1: Photograph of experimental set-up with mannequins facing forwards, toward the blast. Trials were also conducted with the mannequins facing 45º, sideways and back from the explosive charge.

Instrumentation

Three PCB pressure gauges were mounted in each mannequin's head to investigate the explosive shock wave's interaction with the head. The pressure sensors were located at the crown, ear, forehead and rear of the head (Figure 2). Additionally, four reference side-on pressure gauges were placed at various standoff distances around the explosive. For each test, two reference gauges were placed directly next to each mannequin, another sensor was placed closer, and another further away from the explosive charge (shown in Figure 1).

All instrumentation lines were connected via appropriate power supplies and signal conditioning equipment to a computerized data acquisition system (set to 1 MHz sampling rate). The signals from all the pressure transducers were also filtered to remove spurious signals, using a two-pole Butterworth filter set to 10 kHz.

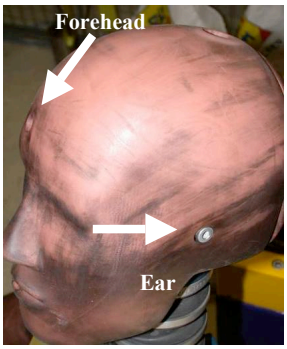

Figure 2: Head pressure transducer mounting locations (rear of the head not shown).

The charge size was determined to create a non-lethal, yet injurious, blast scenario. Table 1 provides the charge masses used in the trial series, with the corresponding IED threat, with casing effects taken into account. Figure 3 provides the theoretical peak pressure and positive phase duration as determined by CONWEP [11] with respect to the blast injury curves set forth by Bass et al. [12]. The smallest charge of 0.75 kg was molded into a sphere, whereas the three larger masses were molded in approximate cylinders with diameter equal to height.

Table 1: Charge mass and IED equivalent

C4 Mass (kg)	Simulated Weaponised IED
0.75	N/A
1.50	US M1 105mm
3.75	Russian OF-56 122mm
5.00	US M107 155mm

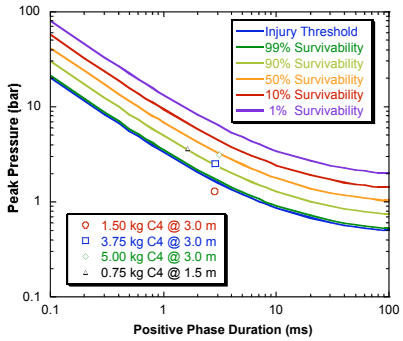

Figure 3: Theoretical overpressures and durations plotted with Bass [12] blast injury curves.

Each mannequin was fitted with a Gentex manufactured, lightweight Marine Corps helmet with a pad-style impact liner (Figure 4). Before each trial, the helmet was repositioned on the mannequin's head to best approximate the manner in which a soldier would commonly wear it. This placed the forehead pressure sensor just below the rim of the helmet. Additionally, a Nomex cover was placed on the face of each mannequin to protect the mannequin's skin from the repeated blasts. The face-cover and the duct tape used to secure it were positioned such that they did not interfere with any of the pressure sensors. Figure 5 provides a pre-blast photo of the mannequin.

Figure 4: Lightweight Marine Gentex combat helmet with pad-style impact liner.

Figure 5: Mannequin with helmet and Nomex face-cover.

EXPERIMENTAL RESULTS

Figure 6 provides the peak pressures and maximum impulses from each reference gauge using the 3.75 kg C4 charges. Both figures also include predictions made from CONWEP [11]. It shows that the C4 charges provided consistent and reproducible pressure profiles, and generally agreed with the CONWEP predictions.

Figure 7 provides the peak filtered pressures from all three pressure gauges using all three charge mass-standoff distance configurations. As expected, the highest peak pressures were noted from the forehead pressure sensor when the mannequin faced forwards. These values are highlighted in Figure 8, where the peak pressure and maximum impulse are plotted with respect to the side-on reference values. Here it can be seen that the forehead pressures follow a linear trajectory close to an equivalent face-on pressure.

In contrast, the highest peak pressures seen for the ear and rear of the head mounted transducers occurred when the mannequin was pointed 45 degrees and sideways to the explosive charge, respectively, not when the sensors within the mannequin faced the charge. The high peak pressure values at the ear from the 45 degree angle (Figure 7) are likely due to the shape of the ear flaps on the helmet, which allow for maximum direct exposure of the sensor to the blast wave. The lower pressure values noted at the rear of the head during backwards-facing trials indicates that mechanisms other than direct transmission of the blast wave through the helmet are at play.

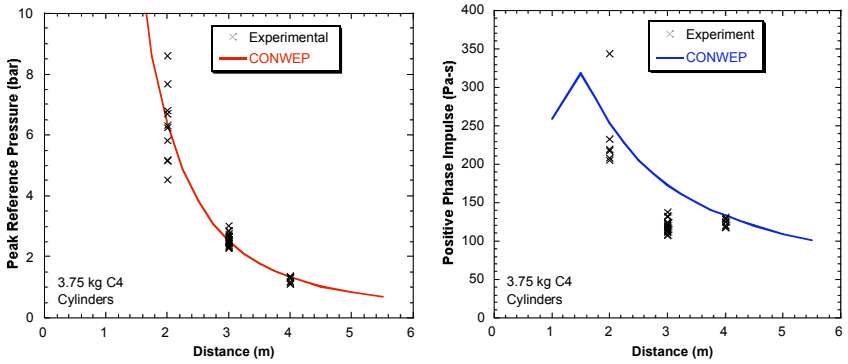

(a) (b)

Figure 6: (a) Reference peak pressure and (b) maximum impulse measurements, also plotted are predictions made by CONWEP for all 3.75 kg C4 trials, respectively.

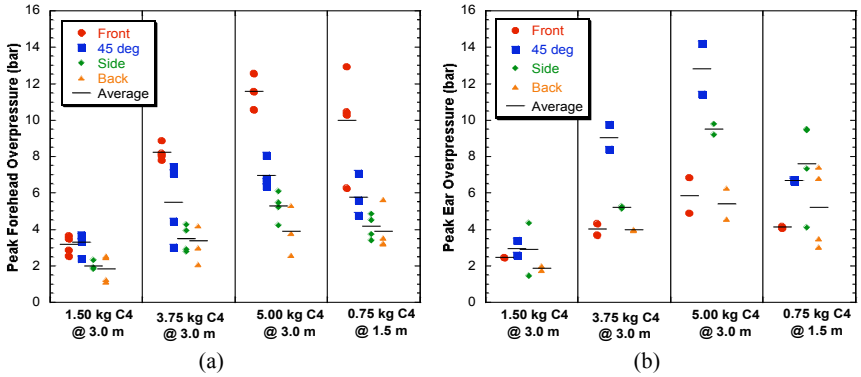

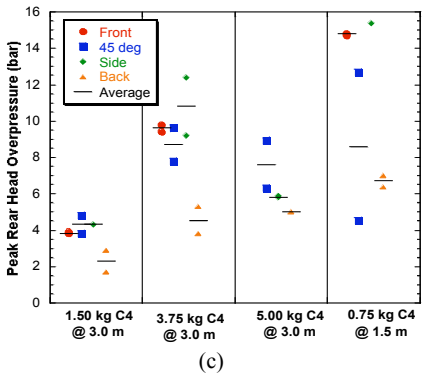

Figure 7: Summary of all peak filtered (a) forehead, (b) ear and (c) rear of head pressures for all four orientations and three charge-standoff configurations.

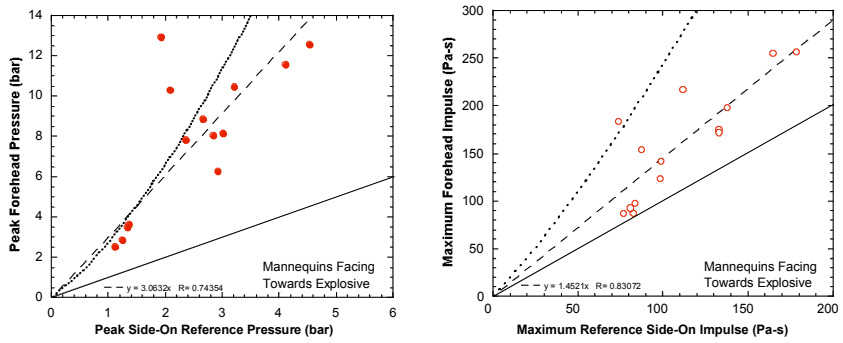

Figure 8: Peak pressure and maximum impulse from the forehead pressure sensor plotted with respect to the (a) peak reference pressure and (b) maximum reference impulse for a mannequin facing the front. Also plotted is a linear best-fit line (dashed) through the available data as well as a predicted reflected pressure and impulse (dotted) determined using CONWEP and an equivalency line (solid).

A second trial series was carried out using the same mannequins with and without helmet protection in a smaller laboratory-scale environment. Smaller 0.25 kg C4 charges were detonated at a standoff distance of 1 m using the identical mannequins and instrumentation. This represents a theoretical blast condition similar, but not identical, to 3.75 kg C4 detonated at a standoff distance from the mannequin of 3.0 m. Figure 9 provides the unprotected and protected peak pressures from the forehead, ear and rear of the head, with the mannequin oriented forwards, sideways and backwards. No trials were conducted at a 45º angle from the explosive charge. Figure 9 shows that the forehead sensor rendered similar peak pressures no matter the orientation, as the sensor was partially exposed to the event with the helmet mounted on the mannequin's head. The ear and rear sensors indicated equivalence or reductions in all three orientations. Figure 9d isolates the pressure values from the sensor facing the blast in each of the three orientations. It can be seen that the peak pressure is reduced the greatest in rear-facing trials with the rear of the head sensor. This is likely due to a combination of the increased projected helmet area blocking the shock and having foam padding between the helmet and the head, something that does not exist at the ear location.

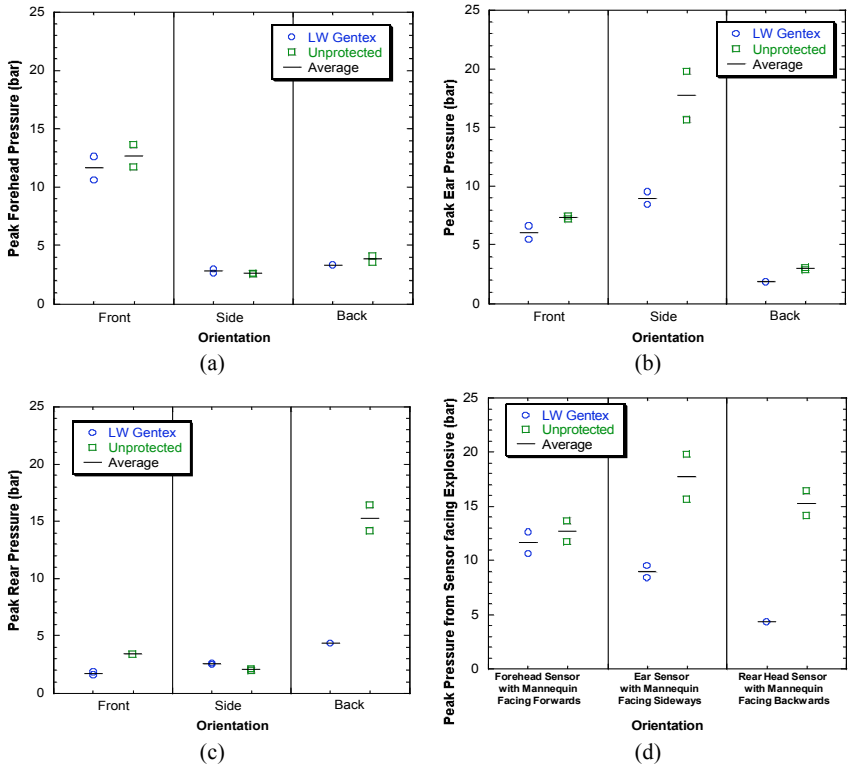

Figure 9: Peak protected and unprotected head pressure values from the (a) forehead, (b) ear & (c) rear of the head during 0.25 kg C4 trials at 1m standoff distance. The peak pressures from the sensor facing the blast in the three different orientations is isolated in (d).

PHYSICAL AND NUMERICAL MODELING

Numerical simulations are used to describe and explain the pressure and flow-field around the head and helmet of a soldier exposed to a blast wave, while comparisons between numerical and experimental results help to validate both methods for further studies and add insight into the physics. The computational modeling procedure is divided into two major steps. First, a blast profile, including the effects of the blast reflection from the ground, is computed assuming cylindrical symmetry and with no mannequin. This separate computation is done with a multi-component, reacting flow model and the FBM-Blast code. The resulting blast profile then provides the boundary conditions for the FAST3D code, which does a three-dimensional unsteady calculation of the flow immediately surrounding the mannequin. A more detailed description of this procedure and the results are given in the following sections.

The governing equations are the compressible Euler equations with species transport:

$$\frac{\partial \rho}{\partial t} + \nabla \cdot \rho \mathbf{v} = 0 \tag{1}$$

$$\frac{\partial \rho \mathbf{v}}{\partial t} + \nabla \cdot \rho \mathbf{v}\mathbf{v} = -\nabla P \tag{2}$$

$$\frac{\partial E}{\partial t} + \nabla \cdot \left(E + P\right)\mathbf{v} = 0 \tag{3}$$

$$\frac{\partial n_k}{\partial t} + \nabla \cdot n_k \mathbf{v} = S_k \tag{4}$$

where ρ is the total density of the mixture, $\mathbf{v}$ is the bulk velocity, E is the total energy, P is the thermodynamic pressure, n_k is the concentration of species k, and S_k is the chemical source for species k. The total enthalpy is:

$$E = \sum_{k=1}^{N} n_k h_k(T) - P + \frac{1}{2}\rho \mathbf{v} \cdot \mathbf{v} \tag{5}$$

where the species enthalpies $h_k(T)$ are computed from 6^{th}-order polynomial curve-fits.

A modified equation of state relates pressure to temperature. For the explosive, a modified equation of state is needed due to the extreme densities immediately after detonation. Since only the pressure relatively far from the explosive is needed, a relatively simple Nobel-Able equation of state is used:

$$P = \frac{n_g RT}{1 - an} \tag{6}$$

where n_g is the concentration of gaseous species, R is the universal gas constant, and a is a parameter chosen that represents the volume taken up by the molecules (taken as $10\ ^{\text{cm}^3}/_{\text{mol}}$).

Modeling C4 Blast Waves

The composition of C4 explosive is approximately 90% RDX ($C_3H_6N_6O_6$) and 10% plasticizer. For these computations, the plasticizer has been ignored. The blast wave is considered to be the result of an RDX charge with 90% mass of the specified experimental charge. Then, the initial density, pressure, and temperature in the explosive volume are calculated assuming a constant-volume decomposition of RDX that has gone to completion. After a detonation, RDX decomposes according to:

$$1kg\ RDX \Rightarrow 13.5074\,H_2O + 6.75371\,CO_2 + 6.75371\,C(s) + 13.5074\,N_2 + 1484.11\,kcal$$

where C(s) is graphite dust. This provides the initial condition of the simulation, which starts with an extremely high concentration of H_2O, CO_2, C(s), and N_2 at high temperature in a very small volume.

Although the calculation of the flow directly surrounding the explosive is not accurate using this approximation, it improves further from the explosive. At distances comparable to the experimental standoff distances, it is very good.

Two global reactions describe the conversion of C(s) and CO to CO_2:

$$C(s) + \tfrac{1}{2}O_2 \Rightarrow CO \text{ , followed by } CO + \tfrac{1}{2}O_2 \Rightarrow CO_2$$

Both reactions are treated as infinitely fast above a temperature of 1000 K, and occur at the contact discontinuity where there is mixing between detonation products and air.

For these computations, the exploded RDX is assumed spherical, with initial conditions shown in Table 2 for the 1.5 kg charge. The gas outside of the explosive is air (79% N_2, 21% O_2) at standard temperature and pressure (298 K, 1.013 bar). This model was used previously in computations for the mitigation of shock waves generated by blasts [13].

Table 2: Initial conditions for 1.5 kg C4 charge.

Amount of C4:	1.5 kg	Temperature:	6,064 K
Density of C4:	1.6 gm/cm³	Pressure:	77.476 kbar
Amount of RDX:	1.35 kg	Gas concentration:	0.0540295 $^{mol}/_{cm^3}$.
Volume of RDX:	843.75 cm³	Radius of RDX:	5.862 cm
H_2O:	18.235 mol 0.0216118 $^{mol}/_{cm^3}$	C(s):	9.1175 mol, 0.0108059 $^{mol}/_{cm^3}$
CO_2:	9.1175 mol 0.0108059 $^{mol}/_{cm^3}$	N_2:	18.235 mol 0.0216118 $^{mol}/_{cm^3}$

The blast model (Eqns. 1-6) with the initial conditions and two-step reaction model described above, is solved using the FBM-Blast code. FBM-Blast is based on the Flux-Corrected Transport (FCT) algorithm [14], which was extended for multidimensional flow-fields [15, 16]. A cylindrical coordinate system is used to capture the reflection off of the ground. An adaptive-mesh-refinement (AMR) method, called PARAMESH [17], is used to provide better resolution around the shock waves and reaction layers while maintaining a coarse mesh in other areas of the grid. Each mesh block size is 16 x 16 cells, and each mesh block can be refined into four smaller blocks during the simulation if it meets specified refinement criteria based on density and pressure. Likewise, derefinement criteria are used to derefine groups of four mesh blocks into one mesh block. For these computations, four levels of refinement are used with cell resolution typically from 4.6875 cm to 0.293 cm for the large cylindrical charges. The computations were run on between 8 to 16 processes of an SGI Altix supercomputer, and generally took between one-half to two hours to run.

Modeling Helmeted-Head Blast Interaction

The three-dimensional simulations of the helmeted-head geometry are computed using the FAST3D code. FAST3D uses the FCT algorithm with spatial splitting [18], and also uses a unique parallelization technique to achieve efficient computation on parallel computers [19]. Flow around the helmeted-head geometry is computed using the Virtual-Cell-Embedding (VCE) procedure [20], where partial cell volumes and interface surface areas are computed using a three-dimensional bitmap of much higher resolution than the computational resolution.

Results from the FBM-Blast simulations are used in the FAST3D simulations as a boundary condition at the inlet plane ($x = 0$). These values determine the inlet plane mass, momentum, energy, and pressure in FAST3D. Since the detonation products do not expand into the Cartesian domain, the three-dimensional model simulates air under perfect gas conditions, reducing the number of conservation equations to three (Eqns. 1-3), and replacing the energy relation (eqn. 5) with

$$E = \frac{P}{\gamma - 1} + \frac{1}{2}\rho \mathbf{v} \cdot \mathbf{v} \tag{7}$$

Figure 10 shows the helmeted-head geometry used in the current study. The geometry is based on the shape of the Advanced Combat Helmet (ACH), but includes no supporting sling structure or pads. There is an uninterrupted gap of about 2.3 cm between the head and the helmet. The helmet data contains 4672 vertices and 9220 triangular surface elements, while the head data contains 1634 vertices and 3264 surface elements. The surface geometry of the head extends down to the sternum and was provided by an outside commercial source [21], and so it is not an exact model of the mannequin. This, and the fact that the face shield used in experiments was not modeled, will lead to differences between experiments and simulations.

The surface data was used to generate a three-dimensional bitmap of the head-helmet geometry with 0.0613 cm resolution in each direction. FAST3D reads in the three-dimensional bitmap, rotates the bitmap to get the correct orientation of the head to the blast, and then extends the base of the head geometry down by 35 cm to represent the torso used in the experiments. Experimental studies show that the head and helmet move very little during the blast impact, thus the model is held rigid during the flow simulation. The simulation computational-cell uses a resolution of 0.25 cm around the helmeted-head, and stretches the grid spacing in the z-direction below the sternum of the head geometry. This resolution results in between 8-10 cells in the gap between the head and the helmet. The overall dimension of the computational domain is 75 cm x 45 cm x 80 cm. The blast propagates in the positive x-direction, and z represents the vertical height. The overall grid size varies dependent on the orientation angle, but a typical grid size is about 300 x 180 x 228 cells, or 12.3 million total cells.

Modeling Helmeted-Head Blast Interaction

The three-dimensional simulations of the helmeted-head geometry are computed using the FAST3D code. FAST3D uses the FCT algorithm with spatial splitting [18], and also uses a unique parallelization technique to achieve efficient computation on parallel computers [19]. Flow around the helmeted-head geometry is computed using the Virtual-Cell-Embedding (VCE) procedure [20], where partial cell volumes and interface surface areas are computed using a three-dimensional bitmap of much higher resolution than the computational resolution.

Results from the FBM-Blast simulations are used in the FAST3D simulations as a boundary condition at the inlet plane ($x = 0$). These values determine the inlet plane mass, momentum, energy, and pressure in FAST3D. Since the detonation products do not expand into the Cartesian domain, the three-dimensional model simulates air under perfect gas conditions, reducing the number of conservation equations to three (Eqns. 1-3), and replacing the energy relation (eqn. 5) with

$$E = \frac{P}{\gamma - 1} + \frac{1}{2}\rho \mathbf{v} \cdot \mathbf{v} \tag{7}$$

Figure 10 shows the helmeted-head geometry used in the current study. The geometry is based on the shape of the Advanced Combat Helmet (ACH), but includes no supporting sling structure or pads. There is an uninterrupted gap of about 2.3 cm between the head and the helmet. The helmet data contains 4672 vertices and 9220 triangular surface elements, while the head data contains 1634 vertices and 3264 surface elements. The surface geometry of the head extends down to the sternum and was provided by an outside commercial source [21], and so it is not an exact model of the mannequin. This, and the fact that the face shield used in experiments was not modeled, will lead to differences between experiments and simulations.

The surface data was used to generate a three-dimensional bitmap of the head-helmet geometry with 0.0613 cm resolution in each direction. FAST3D reads in the three-dimensional bitmap, rotates the bitmap to get the correct orientation of the head to the blast, and then extends the base of the head geometry down by 35 cm to represent the torso used in the experiments. Experimental studies show that the head and helmet move very little during the blast impact, thus the model is held rigid during the flow simulation. The simulation computational-cell uses a resolution of 0.25 cm around the helmeted-head, and stretches the grid spacing in the z-direction below the sternum of the head geometry. This resolution results in between 8-10 cells in the gap between the head and the helmet. The overall dimension of the computational domain is 75 cm x 45 cm x 80 cm. The blast propagates in the positive x-direction, and z represents the vertical height. The overall grid size varies dependent on the orientation angle, but a typical grid size is about 300 x 180 x 228 cells, or 12.3 million total cells.

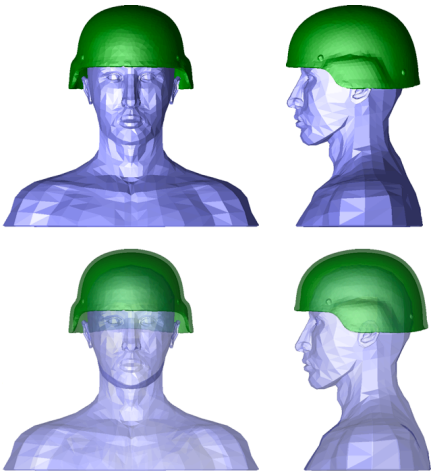

Figure 10: Head and helmet surface arrays used in the simulations.

Figure 11 shows the blast scenario and the domain used in the detailed simulation near the mannequin. The Cartesian domain is aligned with a ray traveling from the center of the blast to the geometric center of the head geometry. Since the spherical wave is approximated as a planar wave in Cartesian space, this alignment more accurately models the direction of the initial pressure wave. The secondary pressure wave that includes the effect of ground reflection approaches the mannequin at a much steeper angle, but in the current calculation this wave is also modeled as a planar wave normal to the domain. The computational results are discussed with these limitations in mind. An improved boundary condition in future work will better represent the shape and direction of the reflected pressure wave.

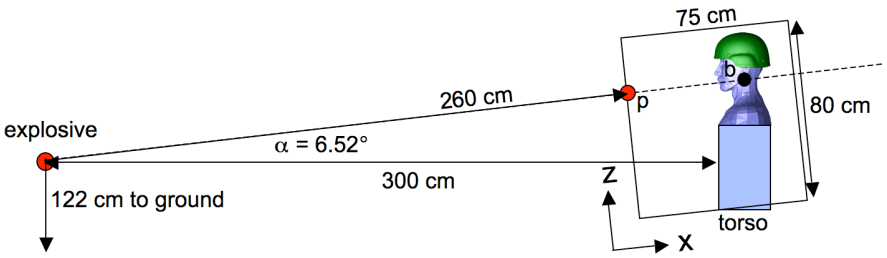

Figure 11: Domain of the detailed simulation relative to the explosive blast.

Computational times for the current three-dimensional simulations using 12 to 24 processors on an SGI Altix are between 4 to 8 hours. Results for the three-dimensional simulations are described using inlet conditions based on the 1.5 kg cylindrical blast case.

COMPUTATIONAL RESULTS

0.75 kg Spherical Charge

Figure 12 shows results for a spherical C4 charge with mass 0.75 kg positioned 1.06 m above the ground. White squares indicate locations of pressure gauges placed 1.0 m, 1.5 m, and 2.0 m from the charge, 1.12 m above the ground, during the corresponding experiment. The domain size for this case is 4.0 m x 4.0 m.

In each frame, pressure and temperature fields are superimposed (pressure, shown by black, with saturation at 4 bar; temperature, shown by red, with saturation at 2500 K). As expected, the front shock wave expands outwards spherically, and then reflects off of the ground. A triple point is created where the reflected and front shock wave meet. The wave between the triple point and the ground is a combination of the front and reflected shock waves and is typically stronger than the front shock wave. The triple point propagates away from the ground along the front shock wave. Spherical blasts also quickly create a low-pressure core due to over-expansion of the detonation products, as is seen in the pressure in Figure 10a. This core of low pressure quickly collapses (Figure 12b), and after the collapse a secondary shock wave expands outwards (Figure 12c-f). The secondary shock wave is independent of the shock wave reflected from the ground and would still be present if the ground were not there. In Figure 10e, the reflected shock wave and the secondary shock wave merge at approximately the height of the pressure transducers, indicating that the second pressure spike seen in the transducer pressure traces arises from a combination of the secondary and reflected shock waves.

In the high temperature region, detonation products mix with air and secondary reactions occur. The density variation between detonation products and air produces instabilities within the reaction layer, and these result in large vortical structures. Figure 13 and Table 3 compare pressure transducer data from the simulations and experiments. Pressure traces at 1.0 m vary significantly, but comparisons are much closer at 1.5 m and 2.0 m. For the numerical case, a clear pressure spike is high, where as it is lost in noise in the experiments (most likely due to the fireball).

There are several sources of error that may cause the differences between experiments and simulations. One is the assumed decomposition of the explosive during the detonation to CO_2 and C(s), instead of CO. This effects the amount of heat released in the detonation as well as the amount of gaseous products produced. Both CO and CO_2 are formed during the detonation of any given explosive. A complicating issue is that, as the detonation products expand and the pressure falls, continuing reactions will change the composition. This may affect the pressure further from the explosive.

The assumption of a constant volume reaction to initialize the computation may also be a source of error. This has been used in a wide range of investigations to approximate the explosive blast, and it appears adequate to compute the first pressure spike. The over-expanded detonation products, and the subsequent collapse of the over-expanded region, are sensitive to conditions near the explosive. This may require a more accurate model than constant volume decomposition.

Another source of error is treating the 10% plasticizer in C4, which does not take part in the decomposition, and so does not add energy to the detonation. It does, however, expand along with the rest of the detonation products, which tends to remove momentum from the detonation. This effect has not been accounted for in the current model, and preliminary indications suggest that this effect is rather small.

Finally, the ground is currently modeled assuming a perfect reflecting surface. An actual ground absorbs some of the blast energy, and this reduces the reflection. In addition, the reflected shock wave may also lift dust and other debris from the ground, which further weakens the reflected shock wave. For the 0.75 kg charge, the ground may be far enough away that the reflection shock wave is insignificant compared to the secondary shock wave. For the larger charges, and the farther standoff distances, this effect is much more important.

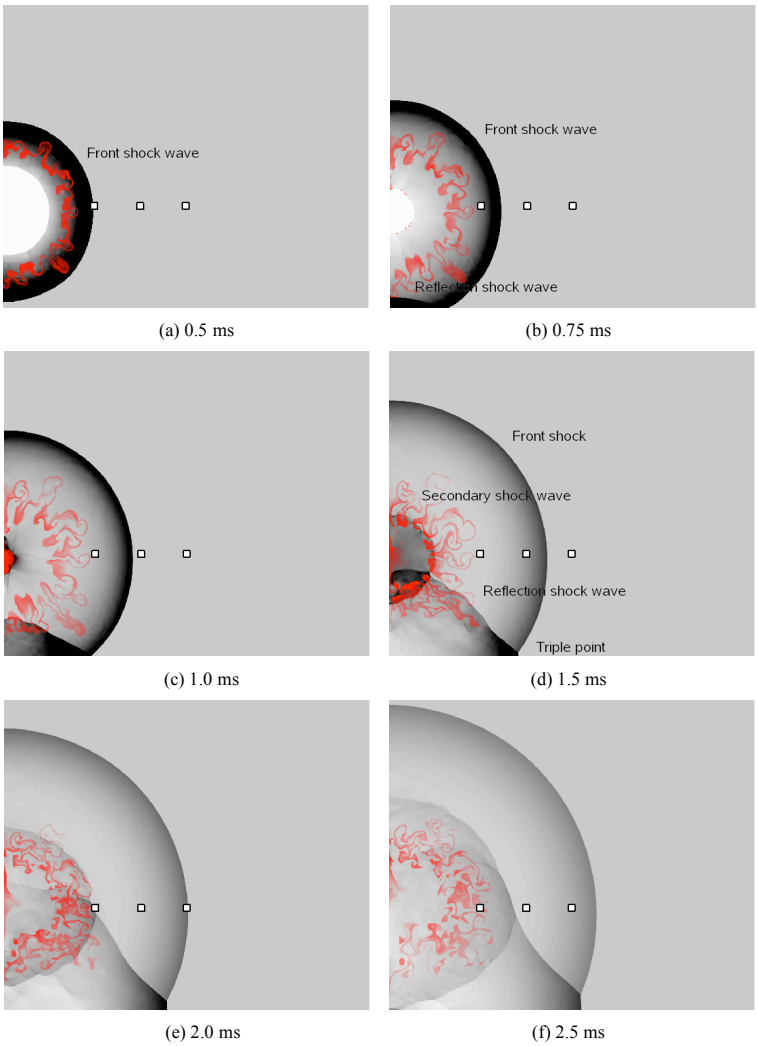

(a) 0.5 ms (b) 0.75 ms

(c) 1.0 ms (d) 1.5 ms

(e) 2.0 ms (f) 2.5 ms

Figure 12: Snapshots of pressure (black) and temperature (red) for 0.75 kg C4 explosive. Pressure transducers are shown at 1.0 m, 1.5 m, and 2.0 m from the explosive and 1.12 m above the ground. Saturation for pressure is 4.052 bar, for temperature is 2500 K.

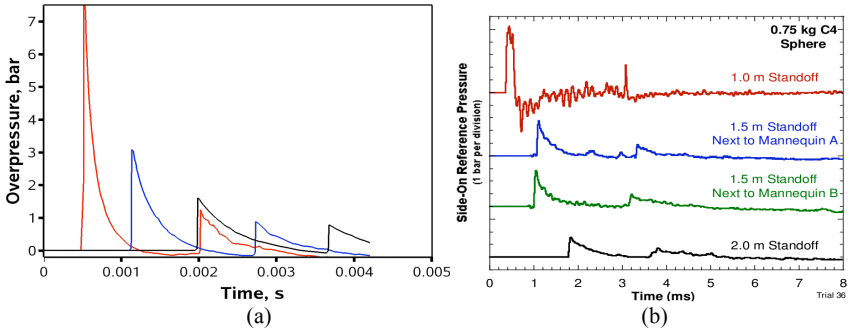

(a) (b)

Figure 13: Comparison of (a) simulation and (b) experimental pressure traces for 0.75 kg C4 charge at 1.0 m, 1.5 m, and 2.0 m standoff distances.

Table 3: Overpressure spike comparison for 0.75 kg C4 charge. Top results are experiment, bottom are simulations.

1.0 m	1.5 m	1.5 m	2.0 m
5.3 bar, 0.5 ms, very noisy	2.85 bar, 1.0 ms 0.93 bar, 3.2 ms	2.73 bar, 1.2 ms 0.86 bar, 3.5 ms	1.58 bar, 1.8 ms 0.74 bar, 3.7 ms
10.15 bar, 0.52 ms 1.27 bar, 2.02 ms	3.10 bar, 1.14 ms 0.90 bar, 2.7 ms		1.62 bar, 1.99 ms 0.81 bar, 3.68 ms

1.5 kg Cylindrical Charge

A comparison of experiments and simulations for the 1.5 kg cylindrical charge at 3.0 m is shown in Figure 14. Because this is used in the study of the helmeted-head geometry, the comparisons agreement at 3.0 m are of particular interest. Figure 14 shows that the simulation captures peak pressures for the two waves, although the timing between the first and second pressure spike is shorter in the simulations. The next subsections discuss the three-dimensional simulations with the mannequin using the blast conditions from the 1.5 kg cylindrical charge.

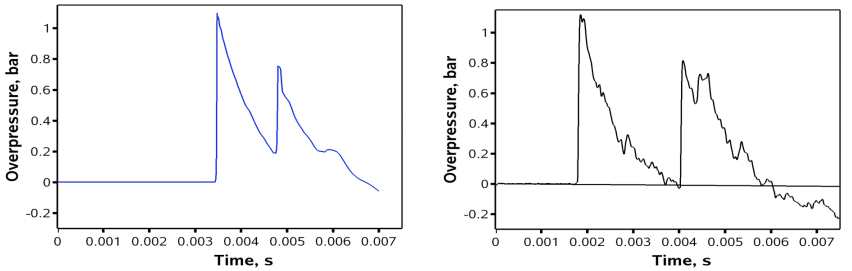

(a) (b)

Figure 14: Comparison of (a) simulation and (b) experimental pressure traces for 1.5 kg C4 charge at 3 m standoff distance. First overpressure spike: 1.11 bar (1.84 ms) for experiment, 1.10 bar (3.48 ms) for simulation; second overpressure spike: 0.78 bar (4.08 ms) for experiment, 0.815 bar (4.80 ms) for simulation.

Front-facing Blast Scenario

Detailed analysis is presented for the front-facing blast resulting from a 1.5 kg C4 charge at 3.0 m standoff distance. Figure 15 shows contours of absolute pressure along the median line and mid-coronal planes for a sequence of times that span the initial and secondary waves striking the geometry. The times listed for each frame are relative to the start of the 3D simulation. The pressure behind the initial shock wave immediately prior to striking the model is 2.2 atm. Due to the angle of incidence, the wave strikes low on the torso first, and the reflected wave produces pressures on the body of 4 atm along the centerline. The highest pressures generated by this reflected shock are in the areas that are directly exposed to the incoming wave and focused by concavity in the surface. Focusing of this wave on the neck between the head and chest (b, c) produces a peak pressure of 7 atm in this region. The helmet protects the covered forehead from the highest pressures resulting from the leading and secondary shock waves, but the high pressure does generate a wave that penetrates the gap (b) and travels underneath the helmet along the median line (c and d) toward the back of the head. Simultaneously, the shock wave travels around the perimeter of the body and helmet. These pressure waves travel faster around the outside of the helmet than underneath the helmet from the front, and the resulting pressure field generates a flow up under the helmet from the sides (c, right). The shock traveling outside the helmet reaches the rear of the helmet before the shock traversing the gap (e), and the pressure waves that have entered the gap from around the helmet focus on a region on the back of the head (f, g). This focusing produces the peak pressures on the head away from the direction of the incident wave when the location is shielded by the helmet.

After this wave focusing generates high pressures under the back of the helmet, the gap acts as a pressurized vessel and drives air out around the helmet perimeter as the high-density air under the helmet expands (h & i). The air under the helmet over-expands to ~0.7 atm during this period. Figure 15i also shows the secondary wave approaching, which reflects (j) with a similar structure as the incident wave (e) but with different magnitude. The focusing at the back of the head is also repeated for the secondary wave, but the magnitude of the peak is considerably lower than the peak for the initial wave. Recall that this secondary wave is approximated in FAST3D as a planar wave approaching along the same ray as the initial wave; the wave in the FBM-Blast calculations actually approaches at a much steeper angle, approximately 25 degrees from the initial wave. The details of wave propagation and subsequent reflections and focusing should be viewed as approximate due to these assumptions.

Pressure histories at selected locations in the computational domain provide quantitative comparison with the experimental data. Figure 16 shows the locations at which pressure histories were recorded: three locations in the forehead region, both ears, and five locations between the crown and the back of the head. Additional locations adjacent to these primary locations but with ~0.5 cm offset away from the surface of the head were used to verify the reported results, but are not shown in Figure 17. All of the rear sensors are under the helmet, as are forehead sensors F1 and F3. Because of geometric variations existing between the computations and the experiments, including the face shield used in the experiments and the precise placement of the helmet on the head, a precise match with experimental results is not expected. In the experiment, the forehead sensor was exposed to the incoming blast between the face shield and the helmet. Sensor F1 was placed to approximate the location of this forehead sensor, but in the computational model the helmet covers this location. Data was collected at both covered and exposed locations to study the sensitivity of the precise sensor and helmet placement.

Figure 15: Pressure contours for selected times for the front-facing blast scenario. Minimum contour (dark blue) = 0.5 atm, black = 1.0 atm, and maximum contour (red) = 3.5 atm.

Figure 17 shows absolute pressure (not overpressure) histories for the front of the head for the forward blast scenario. The computational data is offset in time to match the arrival time of the initial shock wave. Figure 17 shows that the exposed sensor (F2) in the computation experiences an extremely high pressure pulse in the range of 4.5 atm from the reflection of the initial shock wave. The helmet significantly shields the covered sensor (F2), limiting the peak pressure to 2 atm. These peaks bracket the experimental result for the forehead sensor, arriving in the computation earlier than measured in the experiments. This result is consistent with the similar result for the spherical blast modeling described in the previous section and is reinforced by approximating the secondary wave as a planar wave acting in the same direction as the initial wave. Quantitative agreement is good between the peak pressure for the F2 sensor and the experimental data, but this agreement should be viewed cautiously given the approximations made in modeling the secondary wave.

Figure 18 shows the pressure histories at the back of the head for this case, including an expanded view of the initial peaks for this case in the experimental data and two of the computational sensor locations. As in Figure 17, the computational traces have been shifted in time to correlate with the arrival of the initial wave in the experiment. The experimental data demonstrates a double peak when the pressure initially rises followed by a third broader and shorter peak. A double peak can occur when two pressure waves, approaching the point from two directions, arrive at slightly different times. The computation predicts a double peak for location R4, with the first peak caused by a wave transmitted up from behind and below the helmet by the initial shock wave passing around the outside of the helmet. The second wave to reach R4 was the wave transmitted along the median line under the helmet from the front. Sensor R2 was located slightly higher on the head, and these two waves arrived at sensor R2

at almost the same time, producing a significantly higher peak pressure at R2 than at R4. The double peak exhibited by the experimental data suggests that two distinct waves are reaching this sensor as well, one of which is possibly transmitted under the helmet despite the presence of the support system.

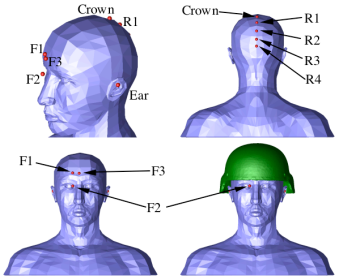

Figure 16: Sensor locations for the computational data.

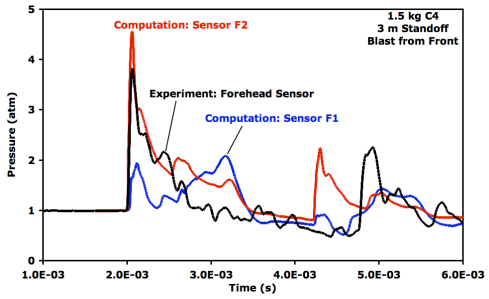

Figure 17: Forehead pressure traces for the forward blast scenario.

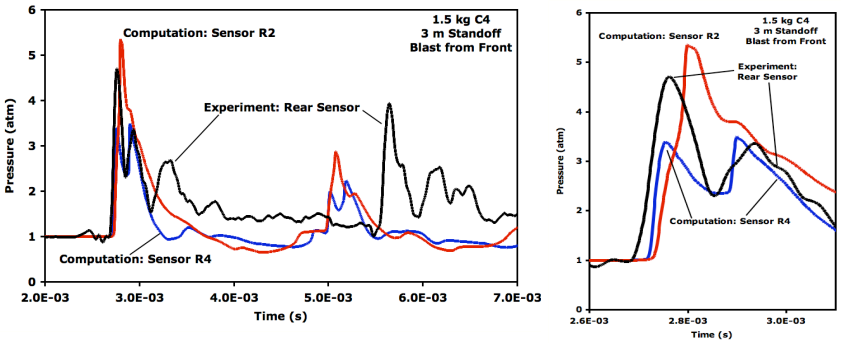

(a) (b)

Figure 18: Rear pressure traces for the forward blast scenario. Initial peaks are highlighted in (b).

Side and Back-facing Blast Scenarios

Figures 19 and 20 show the pressure contour plots for the same spacing but with the blast approaching the model from the rear and from the side, respectively. The same general focusing phenomena is observed in all of the cases, with approximately 5 atm pressure observed in all cases under the helmet on the side of the head away from the blast origin. Figures 19c-g and 20c-f provide an excellent view of the waves enveloping the helmet while simultaneously penetrating the gap from the blast side, and the subsequent intersection of these waves on the leeward side of the head to generate this high pressure region.

Figure 19: Pressure contour plots for the backward blast case.

Figure 20: Pressure contours for the side blast scenario.

SUMMARY AND CONCLUSIONS

Coordinated experimental and computational studies provided cross-validation and gave deeper understanding of the flow physics involved when a blast impinges on a helmeted head. Trials were conducted using four different masses of explosive C4 charges (0.75 kg, 1.5 kg, 3.75 kg and 5.0 kg) at two standoff distances (1.5 m and 3.0 m). The charge configurations were chosen to match typical injurious but non-lethal blasts.

Experimental trials were conducted using two half-Hybrid III mannequins wearing a standard lightweight Gentex helmet. The mannequins were instrumented with three pressure sensors at the forehead, ear and rear of the head. Additionally, four side-on reference gauges were placed at different distances around the charge site to quantify the blasts. Numerical modeling was done using a two-step approach. First, the blast and ground reflection were computed using a multi-component, reacting flow model. Second, the results were used to specify the boundary conditions for a three-dimensional unsteady simulation of the head-helmet complex subjected to a blast wave. Experiments and simulation results were verified and found to be consistent with one another and with other well known blast wave models. These results have shown that the two-step approach used in the computations achieves a good balance between efficiency while maintaining good accuracy.

The forehead pressure sensor, which in the experiments was directly exposed to the blast, rendered results typical of a head without a helmet. The two other sensors, which were covered underneath the helmet, indicated the highest pressures when the mannequin faced 45º from the explosive charge. A second set of laboratory-scale trials quantified the pressure reduction afforded by the helmet. When the unprotected and helmeted pressure measurements from the sensor facing the blasts in each of the three orientations trials were compared, the greatest reductions were noted from the rear sensor in back-facing trials. The results showed that in general the presence of a helmet does reduce primary blast injuries. The computations show that pressure waves focusing in the gap between the helmet and head produce high pressures on the side of the head away from the blast. The experimental data is consistent with this prediction within the variations expected due to differences in the tested geometries and the modeling approximations.

Further research includes extending the computational model to include sling or pad support systems holding the helmet on the head, improving the boundary conditions in the FAST3D code to better represent the blast results, obtaining a better representation of the ground reflection using the FBM-Blast code, and studying more orientations between the helmeted-head and the blast.

ACKNOWLEDGEMENTS

The authors would like to thank Gary Proulx and James MacKiewicz of the US Army Natick Soldier RD&E Center for the helmet scan used in the computational model, and Alan Leung of NRL for generating the 3-D solid geometry and surface mesh of the helmet. The computational work is funded by Office of Naval Research and the United States Marine Corp Systems Command. On the experimental side, the authors would like acknowledge the extensive work of Doug Bueley and Terry Rohachuk from Allen Vanguard. Thanks must also go Rick Guilbeault, Don Wilson, Dean Newfer and Brian Beard of the Canadian Explosives Research Laboratory. The views expressed in this paper are those of the authors and do not represent opinion or policy of the United States Navy, Department of Defense, or Federal Government.

REFERENCES

[1] KH Taber, DL Warden & RA Hurley, *Blast-related Traumatic Brain Injury*, Journal of Neuroscience – Clinical Neuroscience, Spring 2006, Vol. 18, Issue 2, pp 141-145

[2] EG Blackman, ME Hale & SH Lisanby, *Toward Improving TBI Protection Measures and Standards for Combat Helmets,* Institute for Defense Analyses, Defense Science Study Group, 2006-2007 Papers.

[3] J Versace, A Review of the Severity Index, Proceedings of the Fifteenth Stapp Car Crash Conf., pp. 771-796, 1971.

[4] P Prasad, HJ Mertz, The Position of the United States Delegates to the ISO Working Group 6 on the Use of HIC in the Automotive Environment, SAE Paper Number 85-1246, Society of Automobile Engineers, Warrendale, PA, 1985.

[5] A Makris, J Nerenberg, JP Dionne (2000), *Reduction of Blast Induced Head Acceleration in the Field of Anti-Personnel Mine Clearance*, International Research Council on the Biomechanics of Impact (IRCOBI) Conference on the Biomechanics of Impact, Montpellier, France

[6] CR Bass, M Davis, K Rafaels, S Rountree, RM Harris, W Andrefsky, G Dimarco & M Zielinski, *A Methodology for Assessing Blast Protection in Explosive Ordnance Disposal Bomb Suits*, International Journal of Occupational Safety and Ergonomics 2005, Vol. 11, No. 4, pp. 347-361

[7] I Cernak, J Savic, Z Malicevic, *Involvement of the CNS in the General Response to Pulmonary Blast Injury*. Journal of Trauma 1996; Vol.40, pp. 100–104

[8] I Cernak, Z Wang, & J Jiang, *Ultrastructural and Functional Characteristics of Blast Injury-Induced Neurotrauma*, Journal of Trauma 2001; Vol. 50, pp. 695–706

[9] I Cernak, Z Wang, J Jiang, *Cognitive Deficits following Blast Injury-Induced Neurotrauma: Possible Involvement of Nitric Oxide*. Brain Injuries 2001; Vol. 15, pp. 593–612

[10 RJN Garth, *Blast Injury of the Ear*, Scientific Foundations of Trauma, GJ Cooper editor, Oxford: Butterworth-Heinemann Publisher, 1997, pp. 225-235

[11] C Kingery & G Bulmarsh, *Airblast Parameters from TNT Spherical Air Burst and Hemispherical Surface Burst*. ARBRL-TR-02555, US Army Ballistic Research Laboratory, Aberdeen Proving Ground, MD., 1984.

[12] CR Bass, K Rafaels & R Salazar, *Pulmonary Injury Risk Assessment for Short-Duration Blasts*, Proceedings from the Personnel Armour Systems Symposium PASS 2006, Leeds, U.K., September 18th-22nd, 2006

[13] DA Schwer & K Kailasanath, **"**Numerical Simulation of the Mitigation of Unconfined Explosions Using Water Mist*," Proc Combust Inst*, Vol. 31, No. 2, pp. 2361-2369, 2007

[14] JP Boris & DL Book, "Flux Corrected Transport I. SHASTA, A fluid transport algorithm that works." *J Comput Phys*, Vol 11 (1): 38-69, 1973.

[15] ST Zalesak, "Fully multidimensional flux-corrected transport algorithms for fluids." *J Comput Phys*, Vol 31: 335, 1979.

[16] CR DeVore "An Improved Limiter for Multidimensional Flux-Corrected Transport." NRL Technical Report NRL/MR/6440--98-8330, Naval Research Lab, 1998.

[17] P MacNeice, KM Olson, C Mobarry, R deFainchtein, & C Packer, *Comp Phys Commun*, Vol 126, pp. 330-354, 2000.

[18] JP Boris, AM Landsberg, ES Oran, & JH Gardner, "LCPFCT—A Flux-Corrected Transport algorithm for solving generalized continuity equations." NRL Technical Report NRL/MR/6410—93-7192, Naval Research Lab, 1993.

[19] TR Young, AM Landsberg, & JP Boris, "Implementation of the Full 3D FAST3D (FCT) Code Including Complex Geometry on the Intel iPSC/860 Parallel Computer," *Proc 1993 Soc for Computer*

[20] AM Landsberg & JP Boris, AIAA Paper No. 97-1982, 1997.

[21] TurboSquid, http://www.turbosquid.com/.

End of Appendix